Notice

This manuscript is submitted to EarthArXiv and has not yet been peer reviewed. Please note that following peer-review, subsequent versions of this paper may have slightly different content. If accepted for publication, the final version of this pre-print will also be made available. Please feel free to contact the corresponding author directly, we welcome any constructive feedback.

Segment tip geometry of sheet intrusions, II: Field observations of tip geometries and a model for evolving emplacement mechanisms

Tara L. Stephens[1], Richard J. Walker[1], David Healy[2], Alodie Bubeck[3],

[1] School of Geography, Geology and the Environment, University of Leicester, Leicester, LE1 7RH, UK
[2] School of Geosciences, King's College, University of Aberdeen, Aberdeen, AB24 3UE, UK
[3] Lettis Consultants International, Inc., California, USA

Correspondence to: Tara Stephens (tlsteph10@gmail.com)

Abstract

Igneous sheet intrusions are segmented across several orders of magnitude, with segment tip geometry commonly considered indicative of the propagation mechanism (brittle or non-brittle). Proposed propagation mechanisms are inferred to represent host rock mechanical properties during initial magma emplacement; typically, these models do not account for segment sets that show a range of tip geometries within the same lithology. We present a detailed structural characterization of basaltic sill segments and their associated host rock deformation from the Little Minch Sill Complex, Isle of Skye, UK, and a broader comparison with segment geometries in three additional intrusive suites (Utah, USA; and Mull and Orkney, UK). Each separate host lithology shows multiple tip geometries and styles of host rock deformation, from elastic-brittle fracture, to viscous indentation and fluidisation. We attribute this range of host rock deformations to evolving conditions that occur at the tips both during sheet growth and arrest.

Non-Technical Summary

Magma commonly moves through Earth's crust within sheet-like plumbing systems. These sheets start as short segments, which grow and link through time. Underground magma plumbing system growth cannot be observed directly: Much of our understanding of sheet growth comes from excavated and long-since cooled remnants of extinct volcanoes. The way

that sheets grew is typically inferred from their shape, and the way in which the surrounding rocks were broken (deformation) to allow magma to flow through. Current models invoke growth by a single style of rock deformation. Here, we analyse exposed magmatic segments at four different locations, each of which show numerous sheet shapes, and styles of rock deformation. We attribute these features to local changes in the magma and rock properties during and after sheet growth. Our results have direct implications to the mechanics of active magmatic plumbing systems, as the signals of magma propagation may change over time.

1 Introduction

Magmatic sheet intrusions, such as sills and dykes, play a fundamental role in magma transport through the Earth's crust. Field observations, seismic surveys, and analogue models have revealed that sheet intrusions are commonly segmented across several orders of magnitude in scale, from centimetres to kilometres [e.g. Pollard et al., 1975; Hansen and Cartwright, 2006; Wyrick et al., 2014]. Segment geometry is typically linked to a mechanism of propagation, by association with host rock deformation. However, the process of intrusion, and therefore the causal link to geometry, cannot be directly observed in nature. Instead, remote sensing methods such as monitoring seismicity and ground deformation are used to infer mechanisms of host rock deformation in the shallow crust [e.g. Biggs et al., 2009; Ágústsdóttir et al., 2016; Magee et al., 2018]. Remote methods are informed by field observations, hence preserved magmatic networks are critical in our understanding of the mechanism(s) of magma propagation, and the likely signatures of emplacement.

Traditionally, magmatic segments have been treated as Mode I hydrofractures, and their propagation simplified within a Linear Elastic Fracture Mechanics (LEFM) framework: segments are idealised as sheets with tapered (wedge-shaped) tips [e.g. Pollard, 1973; Rubin, 1993]. Many field studies have identified intrusive segments that are not tapered: finger-like forms with rounded (lobate) or blunt tip geometries [e.g. Pollard et al., 1975; Delaney and Pollard, 1981; Hutton, 2009; Schofield et al., 2010; Kavanagh and Sparks, 2011; Spacapan et al., 2017; Walker et al., 2017; Healy et al., 2018; Galland et al., 2019; Kjøll et al., 2019]. Lobate or blunt tips cannot be accommodated elastically, hence LEFM does not hold. This has led to the development of various anelastic propagation models, including viscous indentation and bulldozing [e.g. Spacapan et al., 2017], host rock fluidization [e.g. Schofield et al., 2010], and localised shear-failure and/or ductile flow [e.g. Pollard, 1973; Haug et al.,

2017]. These mechanisms are considered representative of the initial host rock lithology and mechanical properties at the time of magma emplacement [e.g. Schofield et al., 2010; 2012; Spacapan et al., 2017; Haug et al., 2018].

An issue that is generally omitted in intrusion growth models, is that magma and host rock properties can change during the lifetime of an intrusive event [Poppe et al., 2020]. Modifications to the conditions of emplacement during magma propagation, such as increasing magma viscosity during cooling, have been shown to result in modifications to the intrusion geometry and the associated style of host rock deformation for cryptodomes and laccoliths [e.g. Currier and Marsh, 2015; Mattson et al., 2018; Burchardt et al., 2019]. Such modifications are also likely to occur in segmented sheet intrusions, and since late stage processes have the potential to overprint early structures, segment geometries as observed in the field, may be representative only of the final stage of emplacement, rather than the emplacement process as a whole [Walker et al., *in prep*].

Here, we use detailed field observations of intrusive segments to develop a new conceptual dynamic model to account for evolving intrusive segment geometries in a dominantly brittle host rock, due to modifications to the conditions of emplacement. We present examples from four field areas where intrusive segments display different tip geometries in the same host rock to highlight that intrusive segment geometry and the style of host rock deformation may vary with changes to the conditions of emplacement. Segments observed in the field provide a snapshot of the final conditions of the arresting intrusion process.

2 Background

2.1 Mechanisms of segment propagation and resulting geometry

Propagation mechanisms are currently split into two main groups: elastic-brittle and non-brittle. This section summarises the key models of intrusive segment propagation and their associated styles of host rock deformation. Several factors influence the propagation mechanism, including host rock properties such as lithology [e.g. Schofield et al., 2012], degree of compaction [Schofield et al., 2010], and cohesion [Schmeidel et al., 2017] and elastic moduli (e.g. Young's modulus, E; Poisson's ratio, ν; and shear modulus, μ [e.g. Haug et al., 2017, 2018]. Other factors affecting emplacement mechanism include the magma

viscosity [Mattsson et al., 2018; Burchardt et al., 2019; Wilson et al., 2019], magma driving pressure relative to the tectonic stress [Gill and Walker, 2020], the depth of emplacement (Gill and Walker, 2020), and the remote stress state [e.g. Pollard 1973; Pollard et al., 1975; Rubin, 1993; Chanceaux and Menand, 2016; Walker and Gill, 2020].

Elastic-Brittle tip-zone Models

Dyke and sill segment propagation has been considered traditionally as an elastic-brittle deformation (**Fig. 1a-b**). Two models have been proposed: (1) the elastic-splitting model (**Fig. 1a**; [Pollard, 1973]), and (2) the Barenblatt-cohesive zone model (**Fig. 1b**; [Rubin, 1993]). *The Elastic Splitting Model* conforms to linear elastic fracture mechanics (LEFM), where fractures have slit-like geometries with sharp wedge-shaped (tapered) tips (**Fig. 1a**; e.g. Pollard [1973]), as with hydrofracture propagation. This occurs when the driving fluid pressure ΔP (the total fluid pressure (P_f) minus the normal stress (σ_n) acting on the fracture plane) equals or exceeds the tensile strength (σ_T) of the host rock ($\Delta P \geq \sigma_T$). In this model, the host rock bends to accommodate the intrusion thickness; host rock layer thickness above and below the intrusion remains constant. The stress intensity factor (K) at the crack tip is >0, and anelastic deformation at the tip (the plastic process zone) is small relative to the length of the intrusion [Rubin, 1993]. Elastic splitting is linked to emplacement in brittle host rock at low confining stress and temperatures, or at high strain rates under high confining stress [Pollard, 1973].

The Barenblatt-Cohesive Zone Model builds upon the elastic splitting model to include a cohesive process zone at the intrusion tip (**Fig. 1b**). Cohesive stresses act to resist dilation and are on the order of the host rock tensile strength, such that the stress intensity (K) at the crack tip is reduced toward zero (**Fig. 1b**; [Rubin, 1993]). During propagation of a bladed magma-filled fracture, the average flow velocity of the magma in the direction of propagation approaches the tip velocity [Rubin, 1995]. In this condition, the pressure gradient $\frac{\Delta P}{dx}$ (where dx is the along-intrusion dimension) varies approximately as $\frac{1}{t^2}$, hence the magma should lose its pressure within the very narrow tip region, leaving a gap between the viscous magma and the physical fracture tip [Barenblatt, 1962]. This zero-pressure cavity may become filled with exsolved volatiles from the magma, or from inflow of host rock pore fluids [e.g. Pollard, 1973; Lister, 1990; Rubin, 1993, 1995]. Inflow of pore fluids may cause non-localised inelastic damage in the process zone ahead of the intrusion, which increases the energy required for continued fracture propagation [Rubin, 1993; Gudmundsson, 2011].

However, the pressure gradient arising from low pressure in the cavity also serves to drive magma flow toward the tip [Gill and Walker, 2020]. Importantly in the Barenblatt model, if the magma driving pressure cannot facilitate further propagation of the fracture plane, the driving pressure will instead be accommodated by inflation and rounding of the magma front, without an increase in fracture length.

Non-brittle tip-zone models

During non-brittle magma propagation, the host rock behaves as a ductile or viscous medium ahead of the propagating tip. Viscosity contrasts influence the style of host rock deformation: when the magma viscosity exceeds that of the host rock, the magma may behave as a *viscous indenter*, whereas a low viscosity magma intruding into a more viscous host rock may generate a Saffman-Taylor instability, causing the magma front to break down into an array of magma fingers [Saffman and Taylor, 1958]. Two key models of non-brittle magma propagation have been proposed: (1) fluidization, and (2) bulldozing or viscous indentation.

Fluidization is typically attributed to local heating of pore-fluids close to the intrusion, which causes the pore-fluid-pressure to exceed the host rock cohesion, causing disaggregation and flow of the host rock [Kokelaar, 1982; Schofield et al., 2010; 2012]. Accordingly, fluidized host rock is most commonly associated with intrusions emplaced into saturated, unconsolidated or poorly consolidated sedimentary materials that have low or zero cohesion. Fluidisation is most commonly associated with shallow-level intrusions [Kokelaar, 1982; Robertson, 1988; Schofield et al., 2010; 2012; 2014]. Intrusions that propagate via fluidization typically have lobate and/or irregular tip geometries, and are associated with an enveloping zone, or carapace, of fluidized host rock that has lost its internal structure (**Fig. 1c**; [Schofield et al., 2010; 2012; 2014]).

Bulldozing or *Viscous Indentation* models involve host rock buckling, folding, faulting, and/or ductile flow. This deformation results in a thickening of the host rock ahead of a rounded or blunt intrusion tip, of a magnitude similar to the thickness of the intrusion (**Fig. 1d**; [e.g., Pollard, 1973; Merle and Donnadieu, 2000; Spacapan et al., 2017]). Lobate segments with a large width relative to thickness generate large shear and compressive stress concentrations at their tips, which may overcome the shear strength of the adjacent host rock or discontinuities (e.g. bedding planes) to cause bedding plane slip and buckling of strata [Pollard et al., 1975; Rubin, 1993]. Pollard [1973] proposed two end-member models to account for wedge-shaped zones of faulted host rock ahead of rounded segment tips: *brittle-*

shear failure and *ductile-shear failure*, both of which resemble Hencky-relation slip line solutions for a pressurized hole in an infinite plate [e.g., Nadai, 1950; d'Escatha and Mandel, 1974]. Brittle shear failure generates faults oriented ~30° – dependent on the angle of internal friction (ϕ) for the rock – from the maximum local compressive stress (σ_1) about the intrusion tip (**Fig. 1e**), while ductile-shear failure produces faults oriented ~45° from the local σ_1 (i.e., in the plane of maximum shear stress, τ_{max}) (**Fig. 1f**; [Pollard, 1973]). Notably, the segment tip geometry controls the location of shear stress concentrations about the tip [e.g., Obert and Duvall, 1967]. Shear stress will concentrate at the segment tip maximum curvature; in the case of a circular tip this is a single concentration distributed around the tip [e.g., Pollard, 1973, Souche et al., 2019], but in the case of a superelliptical or rectangular tip geometry [e.g., Merle and Donnadieu, 2000; Walker et al., *in prep*], this is not the case.

Pollard [1973] suggested that ductile-shear failure, brittle-shear failure, and elastic splitting models form a spectrum of propagation mechanisms that depend on the confining stress, temperature, pore fluid pressure, and strain rate. Changing one or more of these parameters could therefore result in multiple tip geometries on a single intrusion [for examples see Kjøll et al., 2019; Poppe et al., 2020]. Notably, tip geometries as observed in the field are considered representative of the growing intrusion. Segment geometries observed in outcrop, however, most likely represent the final stage of emplacement (i.e. the 'death' of the segment; Walker et al. [*in prep*]). Hence, intrusive segment geometry – and propagation mechanism – may evolve over the lifespan of a segment. To investigate this theory, we present a detailed characterization of segmented sills in the Little Minch Sill Complex, Isle of Skye.

2.2 Geometrical classification of segmented sheet intrusions

We define individual segments by the length of their semi-axes, with the maximum, intermediate, and minimum semi-axes a ≥ b ≫ c; total segment thickness $t = 2c$, width $w = 2b$, and length $l = 2a$. The spatial relationship between adjacent segments is described by their offset and separation [Delaney and Pollard, 1981]. *Offset* is measured here as the c-axis-parallel distance between the centre-line of adjacent segments; *separation* is the width-parallel distance between the tips of adjacent segments, which may be overlapping, or underlapping. Following Walker et al. [2017] and Healy et al. [2018], we refer to the region

between two adjacent segments as the *relay zone* (termed '*bridge*' by Delaney and Pollard [1981]), and more specifically as either an *overlap zone*, or *underlap zone*. Where segments have linked across the relay zone, it is termed a *breached relay* (cf. '*broken bridge*'*:* Schofield et al. [2010]).

3 Field Observations

Our primary data set is derived from a small (~1.1 km^2) outcrop of segmented sills at Neist Point, Isle of Skye, UK (**Fig. 2a-b**), situated inboard of the eastern North Atlantic volcanic passive margin. The studied sills form part of the Little Minch Sill Complex (LMSC), a ~4000 km^2 sill network emplaced into the Minch Basin between 61-54 Ma, associated with Paleocene magmatic activity during early rifting phases of the North Atlantic (**Fig. 2b**; [Gibb and Gibson, 1989; Saunders et al., 1997; Chambers and Pringle, 2001; Fowler et al., 2004]). Offshore, the LMSC is confined to the Mesozoic sedimentary infill of the Minch Basin, which forms part of a NE-SW striking Mesozoic half-graben system [Roberts and Holdsworth, 1999; Schofield et al., 2016]. No sills crop out in the footwall of the Minch Fault, on the isles of Lewis and Harris. Onshore Skye, the sills predominantly crop out along the northern and north-eastern coastline [Gibb and Gibson, 1989]. Sill geometries along the NE coast of Skye were used by Schofield et al. [2016] to infer that the LMSC propagated eastwards and was fed by a dyke that exploited the basin-bounding Minch fault at depth.

Three thick sills (>10 m thick) crop out in the Neist Point study area and can be traced in section for more than one kilometre (**Fig. 2a-b**). Those sills dip at a low-angle toward the ESE, between 5° and 7° (**Fig. 2c**), and are mildly discordant to bedding, which has an average dip of 4° ESE (**Fig. 2d**). These thick sills are spatially associated with interconnected and cross-cutting networks of thin sills (≤2 m thick) (**Fig. 3**).

Our study focusses predominantly on the network of thin sills shown in **Figure 3**. Here, the sills intrude the Jurassic Leat Shale Formation, which consists of horizontal and interbedded limestones, sandstones, siltstones, and mudstones. The sills also intrude into the base of the Skye Main Lava Series, however due to their inaccessibility we focus only on segments in the sedimentary strata.

The thin sills are exposed in a NE-SW oriented ~20 m high cliff section formed of 3 units: A lower sandstone unit interbedded with thin (cm to tens-of-centimetre thick)

mudstone beds, this is overlain by a mudstone unit, and an upper sandstone unit (**Fig. 3a**). At the level of exposure, the sills occupy ~50% of the total rock volume [Angkasa et al., 2017]. Continuous sheets transgress through the sedimentary sequence as a series of linked offset segments (e.g. segments X-Y-Z on **Fig. 3a**; **Fig. 3b-c**). Non-linked offset and collinear segment arrays are also identified (e.g. **Fig. 3d**); these are the main focus here.

Locally, individual segments are parallel to bedding for short distances. In total, we identified 43 segments; 42% of the identified segments are hosted in mudstone, 35% in sandstone, and 14% in limestone; the remaining 9% are thick segments (>2m) with tips that transect multiple beds (**Fig. 3e**).

Segment pairs display overlapping and underlapping relationships, with offset (en-echelon; **Figs 3a-c, 4a**) and collinear arrangements (**Figs 3d, 4b**). Stepping directions between adjacent offset segments are inconsistent across the study area (compare **Figs 3a-c** and **4a**). Breached relays between offset segments are predominantly formed of single tip-to-plane linkages, noted by an abandoned tip (cf. 'horn': Nicholson and Pollard [1985]) associated with one segment (**Fig. 3b-c**). Breached relays also display near-vertical offset of host rock units across the linkage (**Fig. 3b-c**). Approximately collinear segments, on the other hand, are consistently joined by tip-to-tip links (e.g. **Fig. 3d**). Relay zones between adjacent segments trend NW-SE and NE-SW (**Fig. 3f**); prolate amygdales observed at the upper contact of the lower sill in the key study area (**Fig. 3a**) have long-axes trending NW-SE (**Fig. 3g-h**), suggesting that in this location, the primary magma flow direction was oriented NW-SE, parallel to 61% of the measured relay trends, and perpendicular to the main section. The studied NE-SW oriented outcrop therefore provides an ideal cross-section of the sill segments, and an excellent opportunity to characterise segment geometry as well as the style and distribution of associated host rock deformation.

3.1 Segment geometries and associated host rock deformation

We characterise the two-dimensional (2D) cross-sectional form of individual segments by measuring their thickness (t), width (w), and radius of curvature of the macro-form tip (henceforth ρ_{tip}) from scaled orthorectified photographs (**Fig. 5a**). Pollard et al. [1975] describe ρ_{tip} for an ellipse ($\rho_{tip} = t^2/2w$) and oval ($\rho_{tip} = t/2$) segment geometries (**Fig. 5a**). In the case of a squared ellipse (i.e., superellipses, or Lamé curves: Lamé [1818]), ρ_{tip}

approaches infinity (**Fig. 5a**), though we note that the corners of such geometries also exhibit small ρ values (ρ_{min}) that may act to concentrate stress (**Fig. 5a**; [Greenspan, 1944; Walker et al., *in prep*]).

Following Pollard et al. [1975], the results are plotted and compared to curves for idealised oval and elliptical geometries (**Fig. 5b-c**). The thickness to width (t/w) ratio reflects the overall geometry of the segment, where $t/w \to 0$ represents a thin slit, $t/w \leq 0.2$ represents a sheet, and $t/w \to 1$ represents a magma finger with a near-circular cross-section. The tip geometry is characterised as ρ_{tip} to segment width ratio (ρ_{tip}/w); where sharp tapered (wedge-shaped) tips would plot at $\rho_{tip} = 0$, rectangular tips would plot at $\rho_{tip} = \infty$ [Pollard et al., 1975], and blunt tips with superellipse geometries plot above the oval line.

Of the 43 identified segments, 30 segments could be measured and a total of 47 segment tip geometries were characterised. In some cases, only one segment tip could be measured due to limited exposure or tip-to-plane links between adjacent segments (e.g. segments B-C, **Fig. 4a**). Most of the measured segments display sheet-like geometries (where $0 < t/w < 0.2$; **Fig. 5b**), and predominantly plot between the elliptical and oval lines. All overlapping segments have tapered tips and have ρ_{tip}/w values ≤0.01 (**Fig. 5b**), while underlapping segments display a range of tip geometries from tapered to blunt (superelliptical). Segments with tapered and blunt tip geometries occur within the same host rock lithologies: sandstone (**Fig. 3a-c**), mudstone (**Fig. 4a**), and limestone (**Fig. 4b**). Notably, segments with tapered tips are evenly distributed among the host rock lithologies (e.g. **Figs 3a-c, 4, 5b**). However, most segments with rounded tips are observed in mudstone (**Fig. 5b**). **Figure 5c** shows segment geometry and the style of host rock deformation about the tip. Comparing **Figure 5b** and **5c** shows that segments with tapered tips are associated with deflected bedding around the tapered tip and localised fracturing across all host rock lithologies. Most segments with elliptical to blunt tips are associated with a loss of primary host rock structure.

Figure 5b-c also highlights segment asymmetry denoted by the line length between the data points. Through re-plotting and colour-coding for segments that belong to particular underlapping multi-segment arrays, we find that the segments central to an array are approximately symmetrical about their centre and have oval to blunt tip geometries (**Fig. 6**). Segments nearer the periphery of the array are asymmetrical, with tapered to elliptical distal

tips and proximal tips that approach blunt geometries (**Fig. 6**). This is similar to analogue model results of Pollard et al. [1982] of collinear crack development in an elastic medium (**Fig 6.d**). In their model, tip rounding occurs due to adjacent segments reaching a separation distance at which both segments begin to compete for the available mechanical energy; this competition inhibits Mode I fracture propagation, causing the driving stress to be accommodated via segment inflation and tip rounding.

Notably, **Figure 6c** shows that some segment tips comprise two parts; a light brown chilled glassy outer tip, and a dark finely crystalline inner tip (see also **Fig. 4b**). In most cases the finely crystalline inner tips are more rounded than the chilled glassy outer tips. Segment B of Array 3 comprises two finely crystalline segments enveloped by a chilled glassy margin.

3.2 Host Rock Deformation

The thinly bedded and laminated sedimentary sequence in the Neist Point study area, has laterally continuous units at the scale of outcrop. This is important for identifying the style(s) of host rock deformation associated with each intrusive segment [Spacapan et al., 2017; Galland et al., 2019].

Non-linked, offset, overlapping segments are accommodated consistently by rotation of bedding across the relay zone between adjacent segments (**Fig. 7a-e**), across scales (cm-dam). To compare scales, we measure the host rock rotation angle β, the angle between undisturbed bedding and the rotated bedding orientation in the relay zone. Overlap zones show a negative linear regression for β and the relay zone aspect ratio (calculated as separation/offset) indicates that larger overlaps cause smaller deflections of host rock layering, as would be expected (**Fig. 7h**). Secondary structures (i.e. those that are only found between adjacent segments) also occur, which include: fractures, faults, and intrusive sheets that cross-cut the relay zone (**Fig. 7**). The angle of secondary structures (α) is measured from the plane of the intrusive segment to the plane of the structure [after Tentler and Acocella, 2010]. In the measured overlap zones the angle of secondary structures increases linearly with relay zone aspect ratio (**Fig. 7i**).

Offset underlapping segments also display multiple styles of host rock deformation in the underlap zone. Host rock bending is noted in the underlap zone between adjacent underlapping segments (**Fig. 7g**). Cross-fractures and minor thrust faults in underlap zones

are oriented oblique to sheets with rounded segment tips (**Fig. 7f-g**). Localised zones of brecciated sandstone also occur immediately ahead of rounded segment tips.

Underlap zones between approximately collinear segments in sandstone have lost their primary structure (i.e. bedding and laminations; **Fig. 3d**). In those cases, the segment tips have an overall blunt geometry with local irregularities; small magma fingers extend from the segment tip into the underlap zone towards the adjacent segment (**Fig. 3d**). Similar deformation and segments with rounded to blunt tip geometries with local-irregularities are also observed between underlapping segments in mudstone (**Fig. 8**); here the deformed zone is discoloured relative to the rest of the mudstone unit and small magma fingers also extend from the segment tips into this zone (**Fig. 8b, d, e**). Linked collinear segments are identified by cusps of deformed host rock at the intrusion contact (**Fig. 8c**); similar to those observed by Pollard et al. [1975] for collinear segments in the Shonkin Sag sill, Montana, emplaced into interbedded sandstone and shale units.

Figure 9 shows an approximately 7 m thick sill segment with a rounded to superelliptical tip. Host rock xenoliths occur close to the upper contact of the thick sill segment (**Fig. 9a**), however limited accessibility made it impossible to determine whether these xenoliths are the result of stoping, host rock lenses between stacked sills, or remnant relay zones between linked sill segments. A fold and thrust zone occurs at the western tip (**Fig. 9**). Host rock deformation is most intense at the sill tip, and the deformation intensity decays over a distance of approximately 10 m. Immediately ahead of the sill tip, minor thrust faults accommodate local horizontal shortening and vertical extension (**Fig. 9b-c**); material stacking has caused the thickness of the host rock package to increase by ~49% at the sill tip compared to that at a distance of ~20 m from the sill tip. Ahead of the sill tip major thrust faults (those with lengths >5m) dip away from the sill tip, suggestive of material movement towards and over the sill segment. Minor conjugate thrust fault pairs are also observed at the major thrust faults (**Fig. d-e**). Note that no thrust faults, or significant folding of the host rock, are observed above the intrusion (**Fig. 9a**).

Through plotting the separation and offset for each measured relay zone akin to methods used for dyke and fault analysis (**Fig. 10**; [e.g. Delaney and Pollard, 1981; Fossen and Rotevatn, 2016; Long and Imber, 2011]), we can assess whether segment tip geometry and style of host rock deformation correlate to the spatial relationship between adjacent segments, comparable to the work of Delaney and Pollard [1981]. Collectively, our data spans almost five orders of magnitude for segment offset, ranging from the millimetre to

tens-of-metre scale. All observed overlapping sill segments in the Neist Point study area have asymmetrical tapered tips (and tapered abandoned tips at breached overlaps) (**Fig. 7**; and **A**-**B** on **Fig. 10a**). Only three of the measured overlap zones are intact (i.e. not breached, e.g. **Fig. 7**), and together with the breached overlap zones they fit a positive near-linear power-law regression with an R^2 value of 0.83 (**Fig. 10a**). Underlapping segments, however, display rounded tip geometries at high relay zone aspect ratios (**C**-**D** on **Fig. 10a**), and approaching low relay zone aspect ratios (**E** on **Fig. 10a**). Where the underlap is relatively large (e.g. **C** on **Fig. 10a** has a 20:1 aspect ratio; see also segments E-F on **Fig. 8b**), the zone of host rock deformation is localised about each segment tip and does not extend across the entire underlap zone. For relatively small underlaps (e.g. **D** on **Fig. 10a** has a 5:1 aspect ratio; see also segments F-G and H-I on **Figure 8d-e**) deformation is continuous across the underlap zone; minor magma fingers are observed extending from the adjacent sill tips into this zone. Overall, the underlapping segments display a poor positive correlation between separation and offset (R^2 = 0.29: **Fig 10a**). The poor correlation is likely due to the fact that underlapping segments may stop propagating at any given separation, which is not primarily controlled by the offset.

4 Discussion

4.1 Controls on sheet intrusion tip geometry

Intrusive segment tip geometry and the mechanism of magma propagation are commonly inferred to reflect the mechanical properties of the host rock at the time of initial magma emplacement [e.g. Schofield et al., 2010; 2012; Spacapan et al., 2017; Vachon and Hieronymus, 2017; Bertelsen et al., 2018; Kjøll et al., 2019; Schmiedel et al., 2017; 2019]. These emplacement models are based upon field observations, which preserve the final stage of intrusion. There is, however, the potential for post-emplacement and/or late-stage syn-emplacement overprinting, and the preserved growth mechanism may not be representative of intrusion growth as a whole [see e.g., Spacapan et al., 2017, and Haug et al., 2017]. We can consider the potential for post-emplacement overprinting through detailed field-based textural and structural characterisation of the host rock and intrusion [e.g., Bons et al., 2004]. Few studies have focused on syn-emplacement variations in host rock and magma properties, which may cause a transition in the intrusion tip geometry and emplacement mechanism

[Poppe et al., 2020]. Tapered through to superelliptical sill segments outcrop in the Neist Point study area, within no correlation between host rock lithology and emplacement mechanism (**Fig. 5b-c**). Examples of tapered sill tips are associated with host rock bending, and demonstrate emplacement through elastic brittle processes, at least at the scale of observation (e.g. **Fig. 7a-e**). Elliptical to superelliptical geometries are associated with several styles of localised host rock deformation ahead of the sill segment tips, including fluidisation and brecciation (**Figs 3d, 7f-g, 8**), and shear-band formation (**Fig. 9**).

A similar array of sheet intrusion tip geometries are also observed in a range of host rock types in other locations. The Loch Scridain Sill complex (Isle of Mull, UK) comprises basaltic sill segments with tapered and rounded geometries hosted in subvertically bedded and foliated metasedimentary Moine basement (**Fig. 11a-b**) and horizontal basaltic lavas (**Fig. 11c-f**; see Supplemental File 1 for geological background). Tapered tips are associated with pre-existing fractures and linked offset overlapping segments, while rounded tips are associated with host rock bending in the Moine basement (**Fig. 11a**); and chilled tips (**Fig. 11c-d**) and densely fractured relay zones (**Fig. 11 e-f**) in the lava. Similarly, basaltic sills and dykes in horizontally bedded paralic sandstone-siltstone-mudstone sequences in the San Rafael Sub-Volcanic Field (SRSVF; Utah, USA: **Figs 12** and **13**), and alkaline lamprophyre dykes in horizontally bedded lacustrine and turbiditic sandstone-siltstone-mudstone sequences in Birsay (Orkney, UK: **Fig. 14**) also display tapered and rounded tip geometries in the same host rock units (see Supplemental File 1 for geological background of Utah & Birsay localities). Offset overlapping segments display tapered tips associated with deflected bedding about sill tips in Utah (**Fig. 12a-c**) and deflected subvertical joints about dyke tips in Birsay (**Fig. 14a, d**). In Utah, offset and colinear underlapping segments display rounded to blunt tips, associated with localised host rock brecciation (**Figs 12d-g, 13**), in some cases thin sheets cut obliquely across the brecciated relay zone, emanating from the blunt segment tips (**Figs 12d-g, 13c**; a schematic model for their development is shown in **Fig. 12h**). In Birsay, underlapping segments are associated with localised fracturing in in the tip zone (**Fig. 14b-c, e**). In Mull and Birsay, where the host rock at the segment tip zone is densely fractured, the rounded segment tips also display magma fingers indicative of propagation via viscous fingering (**Figs 11f, 14e**).

Differences in host rock deformation style can reflect the initial host rock shear cohesion and tensile strength [Baer, 1991]. Lithologies with higher shear cohesion are more likely to localise strain into a single fracture, whereas those with low cohesion are not able to

withstand elevated shear stresses, and will fail through distributed fracture along grain boundaries; with increased fluid pressure, disaggregation can lead to fluidization. The scale of the zone of brecciation and fluidisation may therefore relate to the scale of existing discontinuity within the material: In a mudstone, this is the grain size, and in intercalated units (mudstone-sandstone sequences for instance), this may be the layer thickness; in the case of lavas and pre-existing sills, this may be the cooling joint network. All of the observed segments associated with disaggregated (brecciated or fluidized) host rock have elliptical to superelliptical tip geometries. Brecciation and fluidization both act to reduce host rock shear cohesion and tensile strength to zero. Material with low or zero cohesion cannot support tensile stress concentrations; instead, tensile stresses are dissipated as plastic deformation ahead of the intrusion tip [e.g. Mathieu et al., 2008; Bertelsen et al., 2018]. Tensile failure is therefore inhibited, and the segment tip may inflate to accommodate the driving pressure, producing a rounded tip geometry [e.g. Cañón-Tapia and Merle].

Few studies have documented the presence of tapered and rounded segment geometries in the same study area [exceptions include Baer, 1991; Kjøll et al., 2019, Poppe et al., 2020]. Baer [1991] suggests that dykes may propagate in a poorly cemented sandstone by a cyclic process of brittle fracture and viscous fingering that depends on the availability of magma-related fluids and local resistance of the host rock to fluidization. Alternatively, Kjøll et al. [2019] report a 2-stage process to account for dyke geometries in the Scandinavian Caledonides; an earlier set with tapered tips and a later set with rounded tips. They suggest that the later set resulted from magma emplacement into a ductile host due to the thermal effects of the first dyke set locally raising the brittle-ductile transition. Wilson et al. [2016] also suggest a two-stage emplacement model for the Trachyte Mesa intrusions, Henry Mountains, Utah similar to models of Hunt [1953] and Corry [1988]: initial elastic-brittle fracture propagation followed by segment inflation, tip-rounding and associated shear failure of the host rock. In this model, shear failure is caused by overburden flexure and bending once the sill reaches a critical diameter in relation to emplacement depth. The examples presented in our study do not resemble cyclic emplacement processes, and the presence of sharp intrusion contacts and brittle fractures throughout the study areas suggests that in these cases the host rock was primarily brittle. We observe variations in sill tip geometry and styles of host rock deformation for segments varying from cm to tens-of-metre thickness, suggesting that the depth of emplacement and segment size do not necessarily control the final (preserved) geometry or local style of deformation at the segment tip.

During magma emplacement, dynamic changes may modify the properties of the magma and host rock ahead of the propagating tip. Magma viscosity may increase due to cooling, crystallization (and generation of crystal mush), or vesiculation and degassing [e.g. Shaw, 1969; Johnson and Pollard, 1973; Hess and Dingwell, 1996; Currier and Marsh, 2015; Chanceaux and Menand, 2016]. Host rock rheology and cohesion may be altered due to local heating and volatile loss into the host rock [e.g. Aarnes et al., 2011a; 2011b; Annen, 2011; Currier and Marsh, 2015; Chanceau and Menand, 2016; Mattsson et al., 2018]; and localised pore fluid boiling may cause fracturing, brecciation, or fluidization ahead of segment tips [e.g. Pollard, 1973; Pollard et al., 1975]. In their scaling parameters for comparison between natural and modelled intrusions, Galland et al. [2014] suggest that magma viscosity and host rock cohesion are coupled by the dimensionless ratio $\frac{\eta v}{CT}$, where η is magma viscosity, v is flow velocity, C is cohesion, and T is intrusion thickness. This provides a dynamic ratio between time-dependent viscous stresses in the flowing magma and stresses in the host rock; and indicates that increasing magma viscosity has the same effect as decreasing host rock cohesion: inhibits elastic-brittle propagation and promotes tip rounding.

The transition from a tapered to rounded tip geometry would also cause a change in the distribution of stress in the process zone, from a stress singularity at a tapered tip to distributed radial and circumferential stress ahead of an elliptical or oval tip [Pollard, 1973; Souche et al., 2019]. The zones of maximum stress are concentrated at the corners (ρ_{min}) of superelliptical segments, which would likely propagate as viscous indenters causing shear failure of the host (**Fig. 9**; [e.g. Abdelmalak et al., 2012; Guldstrand et al., 2017; Haug et al., 2018; Walker et al., *in prep*]. As the radius of curvature of the corners decreases (i.e. toward a right angle) the stress becomes increasingly localised, and the stress concentration factor (i.e. the ratio of the maximum stress at the contact to the far-field stress: $\frac{\sigma_{max}}{\sigma^{\infty}}$), tends towards infinity [Jaeger et al., 2007; Walker et al., *in prep*]. Propagation of segments with superelliptical to blunt tips, however, is inefficient [Pollard et al., 1975]. Rounded segment tips at the extremities of intrusions, such as those observed in Skye, Mull, Utah, and Orkney are therefore unlikely to represent the initial stages of intrusion growth (i.e., more proximal to source), and are most likely developed later due to modifications to the conditions of emplacement.

4.2 A model for segment evolution

Based on previous propagation models, and our observations of sill segment geometries and associated host rock deformation, we propose a multi-stage model for the evolution of intrusive segment geometry for a basaltic melt in an initially brittle host rock in the shallow crust. Our model accounts for changes to the conditions of emplacement over the lifespan of the segment. We envisage the following stages:

Stage I: Emplacement and propagation as Mode I fractures (**Fig. 15: Stage I**); controlled by periods of driving pressure increase and relaxation following the theory of linear elastic fracture mechanics (LEFM) [e.g. Atkinson, 1987; Cañón-Tapia and Merle, 2006]. Pre-existing planes of weakness (e.g. joints, fractures, bedding, foliation) may be preferentially dilated and intruded during Stage I if the planes are optimally orientated relative to the remote stress state (i.e. oriented normal to the minimum compressive stress) and/or if the magma pressure is sufficiently high to enable dilation of non-optimally oriented planes [Martínez-Poza et al., 2014; Stephens et al 2018]. During Stage I, segments will propagate until the driving pressure is unable to facilitate the next increment of growth; for lateral segment propagation this likely due to local competition for the available mechanical energy between offset and/or collinear adjacent segments [e.g. Pollard et al., 1982], or due to a drop in driving pressure as a function of the increasing segment length for frontal tip propagation. The segment likely accrues the majority of its length and width during this stage.

Stage II: Localised modifications to the conditions of emplacement (**Fig. 15**). This may include modifications to the magma viscosity due to, e.g., volatile loss, degassing, cooling, and crystallization, and/or local modifications to the host rock mechanical properties due heat transfer and/or volatile loss from the magma (increasing the pore fluid pressure ahead of the segment tip). High porosity and/or low cohesion host rock may be fluidized during this stage, whereas cohesive host rock may be fractured or brecciated ahead of the segment tip [Baer, 1991]. Magma degassing and cooling and crystallization cause magma rheology to evolve from viscous to viscoelastic to brittle once chilled [Dingwell, 2006]. During the transition the resistance to flow is increased, which dissipates mechanical energy as viscous drag [Pollard et al., 1975; Rubin, 1993]. The chilled margin may have a higher tensile strength than the host rock, meaning a larger driving pressure would be required to re-establish elastic-brittle propagation [Dingwell, 2006; Currier and Marsh, 2015]. Depending

on the cooling rate relative to the rate of increasing driving pressure, magma flow may become localised into the centre of the segment, cause segment inflation or breaching somewhere along the intrusion, or propagation my cease altogether, in which case the primary tapered tip geometry is preserved (**Figs 4b, 11d**; [Chanceaux and Menand, 2016]). Stage II is therefore associated with stalled propagation, segment inflation, and a change in tip geometry. We envisage minimal change to the segment width during this stage, as the driving pressure is accommodated by segment inflation without further propagation.

Stage III: Minor non-brittle propagation and/or termination. The transition from Stage II to III is marked by renewed propagation (**Fig. 15**). Three scenarios are envisaged for Stage III: (A) flow localisation, (B) breakthrough of the chilled margin to enable resumed Mode I propagation, or (C) renewed propagation via anelastic mechanisms (e.g. viscous indentation, bulldozing, or fluidization). Segment tip rounding during Stage II modifies the local tip stress distribution from a tensile stress singularity to a circumferential tension with radial compression and shear stress concentration. When the width exceeds the thickness of a lobate segment (i.e. a segment aspect ratio (thickness/width) <1), the shear stress concentrations at the tip may facilitate propagation via bulldozing or viscous indentation [Pollard et al., 1975; Rubin, 1993; Soushe et al., 2019]. Local host rock fluidization may enable instigation of a Saffman-Taylor instability at the magma - fluidized host rock interface, for renewed propagation via viscous fingering [Saffman and Taylor, 1958; Pollard et al., 1975]. Segment linkage through a locally fluidized zone may result in a 'cusp' of deformed host rock preserved at the intrusion contact, enabling identification of this mechanism Pollard et al. [1975]. Notably, the renewed propagation mechanism will vary on a segment-by-segment basis, dependent on the changes that occur. Multiple tip geometries and styles of host rock deformation could, therefore, occur in the same host rock units and across a single intrusive complex.

Any further propagation will be governed by the magma driving pressure. We expect the propagation distance during Stage III to be minor relative to Stage I due to the reduction in stress concentration, and inefficiency of shear propagation of a rounded or blunt segment tip relative to a tapered tip (Mode I fracture) [Inglis, 1913; Pollard et al., 1975; Walker et al., *in prep*]. Unless the driving pressure increases significantly to generate a break-out and continued Mode I propagation [e.g. Baer, 1991; Currier and Marsh, 2015: **Fig. 15, Scenario B**] (in which case the process reverts to Stage I), in our model renewed propagation via non-brittle mechanisms represents the final stage in the life of the segment. Hence, the preserved

tip-zone deformation may not be representative of the initial propagation mechanism that controlled the main phase of segment growth.

Notably, our proposed model provides an evolutionary pathway for magmatic segments that do not link during initial brittle propagation. The timescale of tip geometry evolution is dependent on the rate of change to the host rock and/or magma properties. Our model is consistent with observations of sills and dykes ranging from centimetre to tens of metre thickness and emplaced in the brittle crust (up to ~2km depth), so should therefore be consistent with the development of large intrusive complexes, as imaged in subsurface seismic surveys. Importantly, this model provides an explanation as to how multiple styles of host rock deformation, and seemingly multiple propagation mechanisms, occur in a single field area.

Our model applies to emplacement of low viscosity (basaltic) melts at shallow emplacement depths. We note that intrusion of higher viscosity melts (e.g. rhyolite) or magma emplacement at greater confining stresses can cause the initial tip geometry and/or the mechanism of initial host rock deformation to vary from our model. However, in these cases an evolving pathway also occurs [e.g. Currier and Marsh, 2015; Mattson et al., 2018; Burchardt et al., 2019], which is consistent with our findings here.

5 Conclusions

We present a quantitative geometrical characterization of a segmented sill network in the Little Minch Sill Complex, Isle of Skye, UK and compare these data to three additional intrusive complexes: The Loch Scridain Sill Complex, Isle of Mull, UK; sills in the San Rafael Subvolcanic field, Utah; and dykes in Birsay, Orkney, UK. In each study area intrusive segments display tip geometries varying from tapered through to blunt. Multiple styles of host rock deformation were observed from those consistent with elastic-brittle fracture, associated with tapered sill tips, to those consistent with non-brittle propagation models: fluidization, brecciation, and viscous indentation. Our observations suggest that the emplacement mechanism may evolve over the active magmatic lifespan of the segment. We present a conceptual multi-stage emplacement model to account for the variety of segment geometries and styles of host rock deformation observed: elastic-brittle fracture, followed by

localised fluid overpressure at the segment tip, and non-brittle propagation. Non-brittle propagation is likely minor relative to its preservation potential in the rock record: it is representative of the final stages in the life of the segment prior to complete crystallization.

6 Author Contributions

Field data and photographs from were collected by TLS, RJW, AB, and DH. RJW and AB provided valuable discussions in the field, as well as during manuscript preparation, along with DH. TS prepared the manuscript with contributions from all co-authors.

7 Acknowledgements

This work was undertaken during T.L. Stephens's PhD studentship, supported by the Central England Natural Environmental Research Council (NERC) Training Alliance (CENTA) [award reference: 1503848]. The authors would like to thank Mitch Miller for assistance in the field, and Steffi Burchardt and Richard England for constructive comments on an earlier version, which led to significant improvements to the manuscript.

8 Data Availability

Data and supplemental files for this pre-print are available upon request.

9 References

Aarnes, I., Fristad, K., Planke, S. and Svensen, H. (2011a). The impact of host-rock composition on devolatilization of sedimentary rocks during contact metamorphism around mafic sheet intrusions. *Geochemistry, Geophysics, Geosystems, 12*, 1-11. doi: 10.1029/2011gc003636.

Aarnes, I., Svensen, H., Polteau, S. and Planke, S. (2011b). Contact metamorphic devolatilization of shales in the Karoo Basin, South Africa, and the effects of multiple sill intrusions. *Chemical Geology, 281*, 181-194. doi: 10.1016/j.chemgeo.2010.12.007.

Abdelmalak, M.M., Mourgues, R., Galland, O. and Bureau, D. (2012). Fracture mode analysis and related surface deformation during dyke intrusion: Results from 2D experimental modelling. *Earth and Planetary Science Letters, 359–360*, 93-105. doi: 10.1016/j.epsl.2012.10.008.

Ágústsdóttir, T., Woods, J., Greenfield, T., Green, R. G., White, R. S., Winder, T., Brandsdóttir, B., Steinthórsson, S. and Soosalu, H. (2016). Strike-slip faulting during the 2014 Bárðarbunga-Holuhraun dike intrusion, central Iceland. *Geophysical Research Letters, 43*, 1495-1503. doi: doi:10.1002/2015GL067423.

Andrews, S. D. and A. J. Hartley (2015). The response of lake margin sedimentary systems to climatically driven lake level fluctuations: Middle Devonian, Orcadian Basin, Scotland. *Sedimentology, 62*, 1693–1716. doi: 10.1111/sed.12200.

Angkasa, S. S., Jerram, D. A., Millett, J. M., Svensen, H. H., Planke, S., Taylor, R. A., Schofield, N. and Howell, J. (2017). Mafic intrusions, hydrothermal venting, and the basalt-sediment transition: Linking onshore and offshore examples from the North Atlantic igneous province. *Interpretation, 5*, SK83-SK101. doi: 10.1190/int-2016-0162.1.

Annen, C. (2011). Implications of incremental emplacement of magma bodies for magma differentiation, thermal aureole dimensions and plutonism–volcanism relationships. *Tectonophysics, 500***,** 3-10. doi: 10.1016/j.tecto.2009.04.010.

Atkinson, B. K. (1987). Introduction to fracture mechanics and its geophysical applications. *In:* ATKINSON, B. K. (ed.) *Fracture Mechanics of Rock.* London: Academic Press, pp.1-26.

Baer, G. (1991). Mechanisms of dike propagation in layered rocks and in massive, porous sedimentary rocks. *Journal of Geophysical Research, 96*(B7), 11911. doi: 10.1029/91jb00844.

Barenblatt, G .I. (1962). The mathematical theory of equilibrium cracks in brittle fracture. *Adv. Appl. Mech, 7*, 55-129. doi: 10.1016/S0065-2156(08)70121-2.

Bertelsen, H. S., Rogers, B. D., Galland, O., Dumazer, G. and Abbana Benanni, A. (2018). Laboratory Modeling of Coeval Brittle and Ductile Deformation During Magma Emplacement Into Viscoelastic Rocks. *Frontiers in Earth Science, 6*. doi: 10.3389/feart.2018.00199.

Biggs, J., Anthony, E. Y. and Ebinger, C. J. (2009). Multiple inflation and deflation events at Kenyan volcanoes, East African Rift. *Geology, 37*, 979-982. doi: 10.1130/g30133a.1.

Bons, P. D., Druguet, E., Hamann, I., Carreras, J. and Passchier, C. W. (2004). Apparent boudinage in dykes, *Journal of Structural Geology, 26*(4), 625-636. doi: 10.1016/j.jsg.2003.11.009.

Burchardt, S., Mattsson, T., Palma, J. O., Galland, O., Almqvist, B., Mair, K., Jerram, D. A., Hammer, Ø. and Sun, Y. (2019). Progressive growth of the Cerro Bayo cryptodome, Chachahuén volcano, Argentina – implications for viscous magma emplacement. *Journal of Geophysical Research: Solid Earth*. *124*(8), 7– 7724. doi:10.1029/2019jb017543.

Cañón-Tapia, E. and Merle, O. (2006). Dyke nucleation and early growth from pressurized magma chambers: Insights from analogue models. *Journal of Volcanology and Geothermal Research, 158***,** 207-220. doi: 10.1016/j.jvolgeores.2006.05.003.

Chambers, L. M. and Pringle, M. S. (2001). Age and duration of activity at the Isle of Mull Tertiary igneous centre, Scotland, and confirmation of the existence of subchrons during Anomaly 26r. *Earth and Planetary Science Letters, 193*, 333-345. doi: 10.1016/S0012-821X(01)00499-X.

Chanceaux, L. and Menand, T. (2016). The effects of solidification on sill propagation dynamics and morphology. *Earth and Planetary Science Letters, 442***,** 39-50. doi: 10.1016/j.epsl.2016.02.044.

Corry, C. E., (1988). *Laccoliths: mechanics of emplacement and growth*. Geol. Soc. Am. 220. Special Papers.

Currier, R. M. and Marsh, B. D. (2015). Mapping real time growth of experimental laccoliths: The effect of solidification on the mechanics of magmatic intrusion. *Journal of Volcanology and Geothermal Research, 302*, 211-224. doi: 10.1016/j.jvolgeores.2015.07.009.

Delaney, P. T. and Gartner, A. E. (1997). Physical processes of shallow mafic dike emplacement near the San Rafael Swell, Utah. *Geological Society of America Bulletin, 109***,** 1177-1192. doi: 10.1130/0016-7606(1997)109<1177:pposmd>2.3.co;2.

Delaney, P. T. and Pollard, D. D. (1981). Deformation of host rocks and flow of magma during growth of minette dikes and breccia-bearing intrusions near Ship Rock, New Mexico. U.S. *Geol.l Surv. Prof. Paper, 1202*. doi: 10.3133/pp1202.

D'Escatha, Y. & Mandel, J. (1974). Stabilite´ d'une galerie peu profonde en terrain meuble. *Industrie Minerale, Numero Special*, 45–53.

Dingwell, D. B. (2006). Transport Properties of Magmas: Diffusion and Rheology. *Elements, 2*, 281-286. doi: 10.2113/gselements.2.5.281.

Fossen, H. and Rotevatn, A. (2016). Fault linkage and relay structures in extensional settings—A review. *Earth-Science Reviews, 154*, 14-28. doi: 10.1016/j.earscirev.2015.11.014.

Fowler, S. J., Bohrson, W. A. and Spera, F. J. (2004). Magmatic Evolution of the Skye Igneous Centre, Western Scotland: Modelling of Assimilation, Recharge and Fractional Crystallization. *Journal of Petrology, 45***,** 2481-2505. doi: 10.1093/petrology/egh074.

Galland, O., Burchardt, S., Hallot, E., Mourgues, R. and Bulois, C. (2014). Dynamics of dikes versus cone sheets in volcanic systems. *Journal of Geophysical Research: Solid Earth, 119***,** 6178-6192. doi: 10.1002/2014JB011059.

Galland, O., Spacapan, J. B., Rabbel, O., Mair, K., Soto, F. G., Eiken, T., Schiuma, M. and Leanza, H. A. (2019). Structure, emplacement mechanism and magma-flow significance of igneous fingers – Implications for sill emplacement in sedimentary basins. *Journal of Structural Geology, 124***,** 120-135. doi: 10.1016/j.jsg.2019.04.013.

Gartner, A. E. (1986). Geometry, emplacement history, petrography, and chemistry of a basaltic intrusive complex, San Rafael and Capitol Reef Areas, Utah. *U.S. Geological Survey Open-File Report 86- 81*, 112 p. doi: 10.3133/ofr8681.

Gibb, F. G. F. and Gibson, S. A. (1989). The Little Minch Sill Complex. *Scottish Journal of Geology, 25***,** 367-370. doi: 10.1144/sjg25030367.

Gill, S. P. A., & Walker, R. J. (2020). The roles of elastic properties, magmatic pressure, and tectonic stress in saucer-shaped sill growth. *Journal of Geophysical Research: Solid Earth, 125*, e2019JB019041. doi: 10.1029/2019JB019041.

Greenspan, M. (1944). Effect of a Small Hole on the Stresses in a Uniformly Loaded Plate. *Quarterly of Applied Mathematics, 2*, 60-71. doi: 10.2307/43633437.

Gudmundsson, A. (2011). *Rock Fractures in Geological Processes*. Cambridge, Cambridge University Press. doi: 10.1017/CBO9780511975684

Guldstrand, F., Burchardt, S., Hallot, E., and Galland, O. (2017). Dynamics of surface deformation induced by dikes and cone sheets in a cohesive Coulomb brittle crust. *Journal of Geophysical Research: Solid Earth*, *122*, 8511–8524. doi: https://doi.org/10.1002/2017JB014346.

Hansen, D. M. and Cartwright, J. (2006). Saucer-shaped sill with lobate morphology revealed by 3D seismic data: implications for resolving a shallow-level sill emplacement mechanism.(Author abstract). *Journal of the Geological Society*, 163**,** 509. doi: 10.1144/0016-764905-073.

Haug, Ø. T., Galland, O., Souloumiac, P., Souche, A., Guldstrand, F. and Schmiedel, T. (2017). Inelastic damage as a mechanical precursor for the emplacement of saucer-shaped intrusions. *Geology, 45***,** 1099-1102. doi: 10.1130/G39361.1.

Haug, Ø. T., Galland, O., Souloumiac, P., Souche, A., Guldstrand, F., Schmiedel, T. and Maillot, B. (2018). Shear Versus Tensile Failure Mechanisms Induced by Sill Intrusions: Implications for Emplacement of Conical and Saucer-Shaped Intrusions. *Journal of Geophysical Research: Solid Earth, 123***,** 3430-3449. doi: 10.1002/2017JB015196.

Healy, D., Rizzo, R., Duffy, M., Farrell, N., Hole, M. and Muirhead, D. (2018). Field evidence for the lateral emplacement of igneous dykes. *Volcanica*, *1*(2), 85-105. doi: https://doi.org/10.30909/vol.01.02.85105.

Heap, M. J. and Faulkner, D. R. (2008). Quantifying the evolution of static elastic properties as crystalline rock approaches failure. *International Journal of Rock Mechanics and Mining Sciences, 45*, 564-573. doi: https://doi.org/10.1016/j.ijrmms.2007.07.018.

Heap, M. J., Faulkner, D. R., Meredith, P. G. and Vinciguerra, S. (2010). Elastic moduli evolution and accompanying stress changes with increasing crack damage: implications for stress changes around fault zones and volcanoes during deformation. *Geophysical Journal International, 183***,** 225-236. doi: 10.1111/j.1365-246X.2010.04726.x.

Hess, K. U. and Dingwell, D. D. (1996). Viscosities of hydrous leucogranitic melts: A non-Arrhenian model. *American Mineralogist, 81*, 1297-1300 . doi: 10.2138/am-1996-9-1031.

Hutton, D. H. W. (2009). Insights into magmatism in volcanic margins: bridge structures and a new mechanism of basic sill emplacement – Theron Mountains, Antarctica. *Petroleum Geoscience, 15***,** 269-278. doi: 10.1144/1354-079309-841.

Hunt, C.B. (1953). Geology and Geography of the Henry Mountains Region, Utah: *U.S. Geol. Surv. Prof. Paper*, *228*, 234 p. doi: https:// doi .org /10 .3133 /pp228.

Inglis, C.E. (1913). Stresses in Plates Due to the Presence of Cracks and Sharp Corners. *Transactions of the Institute of Naval Architects, 55*, 219-241.

Jaeger, J. C., Cook, N. G. W. and Zimmerman, R. W. (2007). *Fundamentals of Rock Mechanics.* Oxford, Blackwell Publishing Ltd.

Johnson, A. M. and Pollard, D. D. (1973). Mechanics of growth of some laccolithic intrusions in the Henry mountains, Utah, I: Field observations, Gilbert's model, physical properties and flow of the magma. *Tectonophysics*. *18*(3–4), 261-309. doi: https://doi.org/10.1016/0040-1951(73)90050-4.

Kavanagh, J. L. and Sparks, R. S. J. (2011). Insights of dyke emplacement mechanics from detailed 3D dyke thickness datasets. *Journal of the Geological Society, 168***,** 965-978. doi: 10.1144/0016-76492010-137.

Kille, I. C., Thompson, R. N., Morrison, M. A. and Thompson, R. F. (1986). Field evidence for turbulence during flow of basalt magma through conduits from southwest Mull. *Geological Magazine, 123*(6), 693-697. doi: 10.1017/S0016756800024201.

Kjøll, H. J., Galland, O., Labrousse, L. and Andersen, T. B. (2019). Emplacement mechanisms of a dyke swarm across the brittle-ductile transition and the geodynamic implications for magma-rich margins. *Earth and Planetary Science Letters, 518***,** 223-235. doi: https://doi.org/10.1016/j.epsl.2019.04.016.

Kokelaar, B. P. (1982). Fluidization of wet sediments during the emplacement and cooling of various igneous bodies. *Journal of the Geological Society, 139***,** 21-33. doi: 10.1144/gsjgs.139.1.0021.

Lamé, G. (1818). *Examen des différentes méthodes employées pour résoudre les problèmes de géométrie*. Paris, V. Courcier.

Lister, J.R. (1990). Buoyancy-driven fluid fracture: the effects of material toughness and of low-viscosity precursors. *J. Fluid Mech, 210*, 263-280. doi: 10.1017/S0022112090001288.

Long, J. J. and Imber, J. (2011). Geological controls on fault relay zone scaling. *Journal of Structural Geology, 33***,** 1790-1800. doi: 10.1016/j.jsg.2011.09.011.

Magee, C., Stevenson, C. T. E., Ebmeier, S. K. , Keir, D., Hammond, J. O. S., Gottsmann, J. H., Whaler, K. A., Schofield, N., Jackson, C. A-L. Petronis, M. S. O'Driscoll, B., Morgan, J., Cruden, A., Vollgger, S. A., Dering, G., Micklethwaite, S. and Jackson, M. D. (2018). Magma Plumbing Systems: A Geophysical Perspective. *Journal of petrology, 59*(6), 1217–1251. doi: 10.1093/petrology/egy064

Martínez-Poza, A. I., Druguet, E., Castaño, L. M. Castaño, Carreras, J. (2014). Dyke intrusion into a pre-existing joint network: The Aiguablava lamprophyre dyke swarm (Catalan Coastal Ranges). *Tectonophysics*, *630*, 75-90. doi: 10.1016/j.tecto.2014.05.015.

Mathieu, L., Van Wyk De Vries, B., Holohan, E. P. and Troll, V. R. (2008). Dykes, cups, saucers and sills: Analogue experiments on magma intrusion into brittle rocks. *Earth and Planetary Science Letters, 271***,** 1-13. doi: 10.1016/j.epsl.2008.02.020.

Mattsson, T., Burchardt, S., Almqvist, B. S. G. and Ronchin, E. (2018). Syn-Emplacement Fracturing in the Sandfell Laccolith, Eastern Iceland—Implications for Rhyolite Intrusion Growth and Volcanic Hazards. *Frontiers in Earth Science, 6, 5 p*. doi: 10.3389/feart.2018.00005.

Merle, O. & Donnadieu, F. (2000). Indentation of volcanic edifices by the ascending magma. In: Vendeville, B., Mart, Y. & Vigneresse, J.-L. (eds) Salt, Shale and Igneous diapirs in and around Europe. *Geological Society, London, Special Publications, 174*, 43–53. doi: 10.1144/GSL.SP.1999.174.01.03.

Nadi, A. 1950. *Theory of Flow and Fracture of Solids*, 1, McGraw-Hill Book Co, New York.

Nicholson, R. and Pollard, D. D. (1985). Dilation and linkage of echalon cracks. *Journal of Structural Geology, 7***,** 583-590. doi: 10.1016/0191-8141(85)90030-6.

Obert, L., and Duvall. W. I. (1967). *Rock mechanics and the design of structures in rock*. John Wiley and Sons, Inc., New York.

Peterson, F. (1988). A revision of units in the San Rafael Group and the Morrison Formation. *U.S. Geological Survey Bulletin, 1633-B,* B13-56.

Pollard, D. D. (1973). Derivation and evaluation of a mechanical model for sheet intrusions. *Tectonophysics, 19,* 233-269. doi: 10.1016/0040-1951(73)90021-8.

Pollard, D. D., Muller, O. H. and Dockstader, D. R. (1975). The Form and Growth of Fingered Sheet Intrusions. *Geological Society of America Bulletin, 86*(3), 351-363. doi: 10.1130/0016-7606(1975)86<351:TFAGOF>2.0.CO;2.

Pollard, D. D., Segall, P. and Delaney, P. T. (1982). Formation and interpretation of dilatant echalon cracks. *Geological Society of America Bulletin, 93*(12), 1291-1303. doi: 10.1130/0016-7606(1982)93<1291:FAIODE>2.0.CO;2.

Poppe, S., Galland, O., de Winter, N. J., Goderis, S., Claeys, P., Debaille, V., Boulvais, P., and Kervyn. M. (2020). Structural and geochemical interactions between magma and sedimentary host rock: The Hovedøya case, Oslo Rift, Norway. *Geochemistry, Geophysics, Geosystems, 21,* e2019GC008685. doi: 10.1029/2019GC008685.

Richardson, J. A., Connor, C. B., Wetmore, P. H., Connor, L. J. and Gallant, E. A. (2015). Role of sills in the development of volcanic fields: Insights from lidar mapping surveys of the San Rafael Swell, Utah. *Geology, 43,* 1023-1026. doi: 10.1130/g37094.1.

Roberts, A. M. and Holdsworth, R. E. (1999). Linking onshore and offshore structures: Mesozoic extension in the Scottish Highlands. *Journal of the Geological Society, 156***,** 1061-1064. doi: 10.1144/gsjgs.156.6.1061.

Robertson, E. C. (1988). Thermal Properties of Rocks. *U.S. Geological Survey Open File Report 88-441,* 106 p.

Rubin, A. M. (1993). Tensile fracture of rock at high confining pressure: Implications for dike propagation. *Journal of Geophysical Research, 98,* 15919. doi: 10.1029/93jb01391.

Rubin, A. M. (1995). Propagation of magma filled cracks. *Annual Review of Earth and Planetary Sciences, 23***,** 287-336. doi: 10.1146/annurev.ea.23.050195.001443.

Saffman, P. G. and Taylor, G., F. R. S. (1958). The Penetration of a Fluid into a Porous Medium or Hele-Shaw Cell Containing a More Viscous Liquid. *Proceedings of the Royal Society of London. Series A, Mathematical and Physical Sciences, 245,* 312-329. doi: 10.1098/rspa.1958.0085.

Saunders, A. D., Fitton, J. G., Kerr, A. C., Norry, M. J. and Kent, R. W. (1997). The North Atlantic Igneous Province. *In:* J, M. J. & F, C. M. (eds.) *Large Igneous Provinces: Continental, Oceanic, and Planetary Flood Volcanism.* Washington, D. C: American Geophysical Union.

Schmiedel, T., Galland, O. and Breitkreuz, C. (2017). Dynamics of Sill and Laccolith Emplacement in the Brittle Crust: Role of Host Rock Strength and Deformation Mode. *Journal of Geophysical Research: Solid Earth, 122,* 8860-8871. doi: 10.1002/2017JB014468.

Schmiedel, T., Galland, O., Haug, Ø. T., Dumazer, G. and Breitkreuz, C. (2019). Coulomb failure of Earth's brittle crust controls growth, emplacement and shapes of igneous sills, saucer-shaped sills and laccoliths. *Earth and Planetary Science Letters, 510***,** 161-172. doi: 10.1016/j.epsl.2019.01.011.

Schofield, N., Brown, D. J., Magee, C. and Stevenson, C. T. (2012). Sill morphology and comparison of brittle and non-brittle emplacement mechanisms. *Journal of the Geological Society, 169***,** 127-141. doi: 10.1144/0016-76492011-078.

Schofield, N., Alsop, I., Warren, J., Underhill, J. R., Lehné, R., Beer, W. and Lukas, V. (2014). Mobilizing salt: Magma-salt interactions. *Geology, 42*, 599-602. doi: 10.1130/G35406.1.

Schofield, N., Jerram, D. A., Holford, S., Archer, S., Mark, N., Hartley, A., Howell, J., Muirhead, D., Green, P., Hutton, D. and Stevenson, C. (2016). Sills in Sedimentary Basins and Petroleum Systems. *In:* BREITKREUZ, C. & ROCCHI, S. (eds.) *Physical Geology of Shallow Magmatic Systems: Dykes, Sills and Laccoliths. Advances in Volcanology (An Official Book Series of the International Association of Volcanology and Chemistry of the Earth's Interior).* Cham: Springer International Publishing, pp.273-294.

Schofield, N., Stevenson, C. and Reston, T. (2010). Magma fingers and host rock fluidization in the emplacement of sills. *Geology, 38*, 63-66. doi: 10.1130/g30142.1.

Shaw, H.R., (1969). Rheology of basalt in the melting range. *Journal of Petrol*ogy, *10*(3), 510-535. doi: 10.1093/petrology/10.3.510.

Souche, A., Galland, O., Haug, Ø. T. and Dabrowski, M. (2019). Impact of host rock heterogeneity on failure around pressurized conduits: Implications for finger-shaped magmatic intrusions. *Tectonophysics, 765*, 52-63. doi: 10.1016/j.tecto.2019.05.016.

Spacapan, J. B., Galland, O., Leanza, H. A. and Planke, S. (2017). Igneous sill and finger emplacement mechanism in shale-dominated formations: a field study at Cuesta del Chihuido, Neuquén Basin, Argentina. *Journal of the Geological Society, 174***,** 422-433. doi: 10.1144/jgs2016-056.

Stephens, T. L., Walker, R. J., Healy, D., Bubeck, A. and England, R. W. (2018). Mechanical models to estimate the paleostress state from igneous intrusions. *Solid Earth, 9*, 847-858. doi: 10.5194/se-9-847-2018.

Stephens, T. L., Walker, R. J., Healy, D., Bubeck, A., England, R. W. and Mccaffrey, K. J. W. (2017). Igneous sills record far-field and near-field stress interactions during volcano construction: Isle of Mull, Scotland. *Earth and Planetary Science Letters, 478***,** 159-174. doi: 10.1016/j.epsl.2017.09.003.

Tentler, T. and Acocella, V. (2010). How does the initial configuration of oceanic ridge segments affect their interaction? Insights from analogue models. *Journal of Geophysical Research: Solid Earth, 115*. B01401. doi: 10.1029/2008JB006269.

Vachon, R. and Hieronymus, C. F. (2017). Effect of host-rock rheology on dyke shape, thickness and magma overpressure. *Geophysical Journal International, 208***,** 1414-1429. doi: 10.1093/gji/ggw448.

Walker, R.J., Gill, S.P.A. (2020). Tectonic stress controls saucer-shaped sill geometry and emplacement mechanism. *Geology*. *48*(9), 898–902. doi: 10.1130/G47604.1

Walker, R. J., Healy, D., Kawanzaruwa, T. M., Wright, K. A., England, R. W., Mccaffrey, K. J. W., Bubeck, A. A., Stephens, T. L., Farrell, N. J. C. and Blenkinsop, T. G. (2017). Igneous sills as a record of horizontal shortening: The San Rafael subvolcanic field, Utah. *Geological Society of America Bulletin, 129***,** 1052-1070. doi: 10.1130/b31671.1.

Walker, R. J. et al. (*in prep*). Segment tip geometry of sheet intrusions, I: Theory and numerical models for the role of tip shape in controlling propagation pathways.

Wilson, P. I. R., Mccaffrey, K. J. W., Wilson, R. W., Jarvis, I. and Holdsworth, R. E. (2016). Deformation structures associated with the Trachyte Mesa intrusion, Henry Mountains, Utah: Implications for sill and laccolith emplacement mechanisms. *Journal of Structural Geology*, *87***,** 30-46. doi: 10.1016/j.jsg.2016.04.001.

Wilson, P. I. R., McCaffrey, K. J. W., and Holdsworth, R. E. (2019). Magma-driven accommodation structures formed during sill emplacement at shallow crustal depths: The Maiden Creek sill, Henry Mountains, Utah: *Geosphere*, *15*(4), 1368–1392. doi: 10.1130/GES02067.1.

Wyrick, D. Y., Morris, A. P., Todt, M. K., and Watson-Morris, M. J. (2015). Physical analogue modelling of Martian dyke-induced deformation, in Platz, T., Massironi, M., Byrne, P. K., and Hiesinger, H., eds., Volcanism and Tectonism Across the Inner Solar System: *Geological Society of London, Special Publication*, *401*, 395–403. doi: 10 .1144 /SP401 .15.

10 Figures

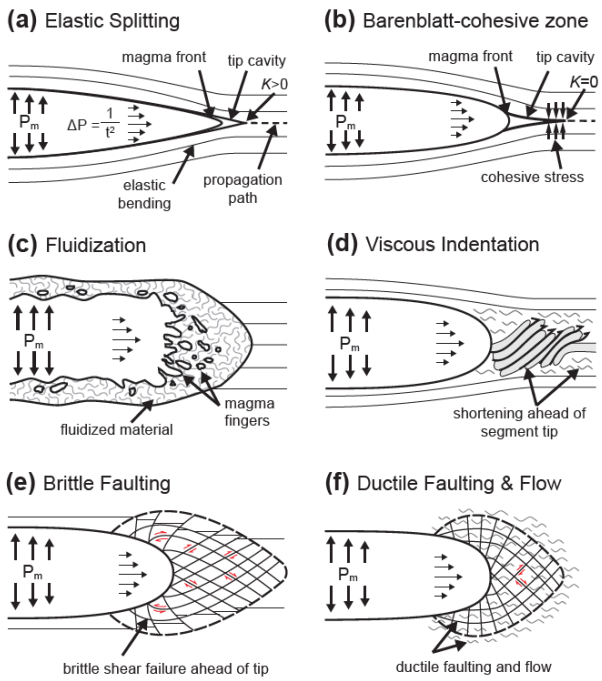

Figure 1. Propagation mechanisms for intrusion emplacement, and the associated host rock deformation and ideal tip geometries. P_m = magma pressure. **(a-b)** Linear elastic fracture mechanics models, (K = stress intensity factor): **(a)** Elastic-splitting model [Pollard, 1973; Rubin, 1993]; **(b)** Barenblatt-cohesive zone model; cohesive stress at the fracture tip acts against dilation [Rubin, 1993]. **(c-d)** Inelastic propagation models: **(c)** thermal fluidization, results in a loss of primary host rock structures (i.e. bedding/ lamination) [e.g. Schofield et al., 2012]; **(d)** viscous-indenter; shortening occurs within one 'weak' unit, e.g. shale [e.g. Spacapan et al., 2017]. **(e)** Brittle faulting model [after Pollard, 1973]. **(f)** Ductile faulting and flow model [after Pollard, 1973].

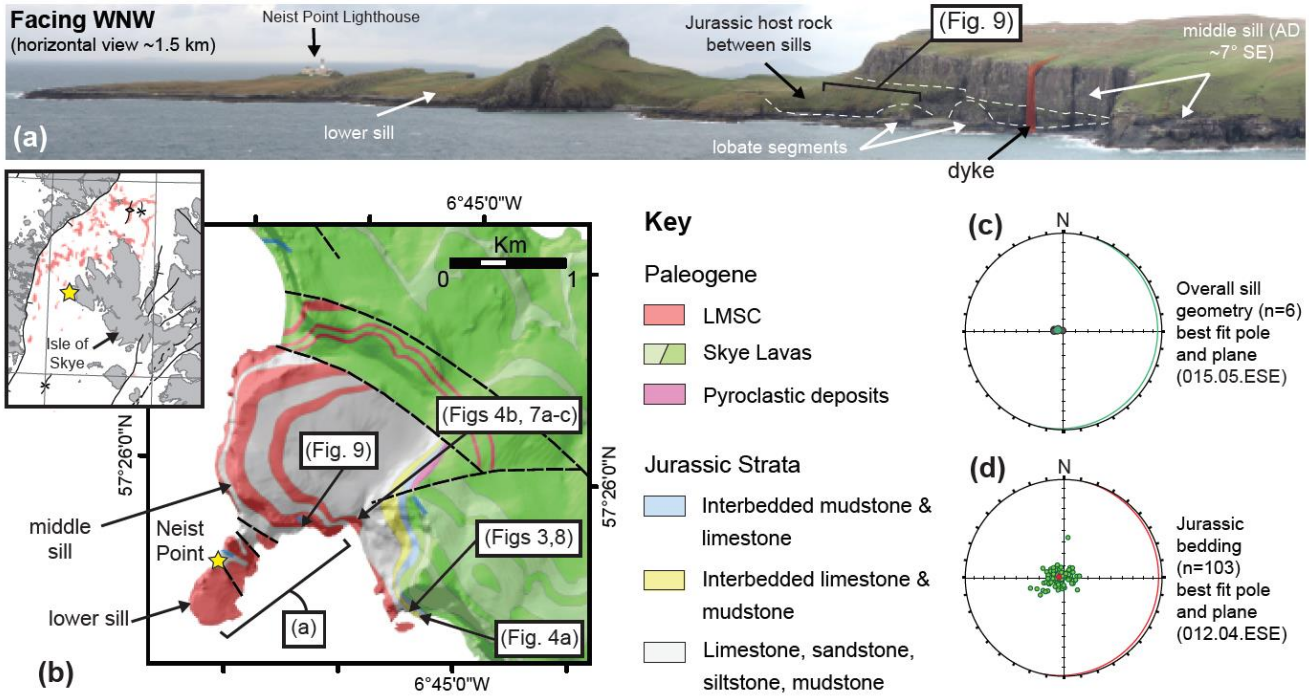

Figure 2. Location of Little Minch Sill Complex study area at Neist Point. **(a)** Overview photograph of Neist Point showing the lower and middle sills (AD = apparent dip). **(b)** Location Map for the Neist Point study area with bedrock geology and figure locations. The inset map shows the location of Neist Point (yellow star) on the Isle of Skye, and the offshore extent of the Little Minch Sill Complex (LMSC). **(c)** Equal area lower hemisphere stereonet plotting the three major sills (grey), with average pole and plane (green), given as strike, dip and dip-direction. **(d)** Equal area lower hemisphere stereonet plotting Jurassic bedding as poles to planes (green), with average pole and plane (red) given as strike, dip and dip-direction.

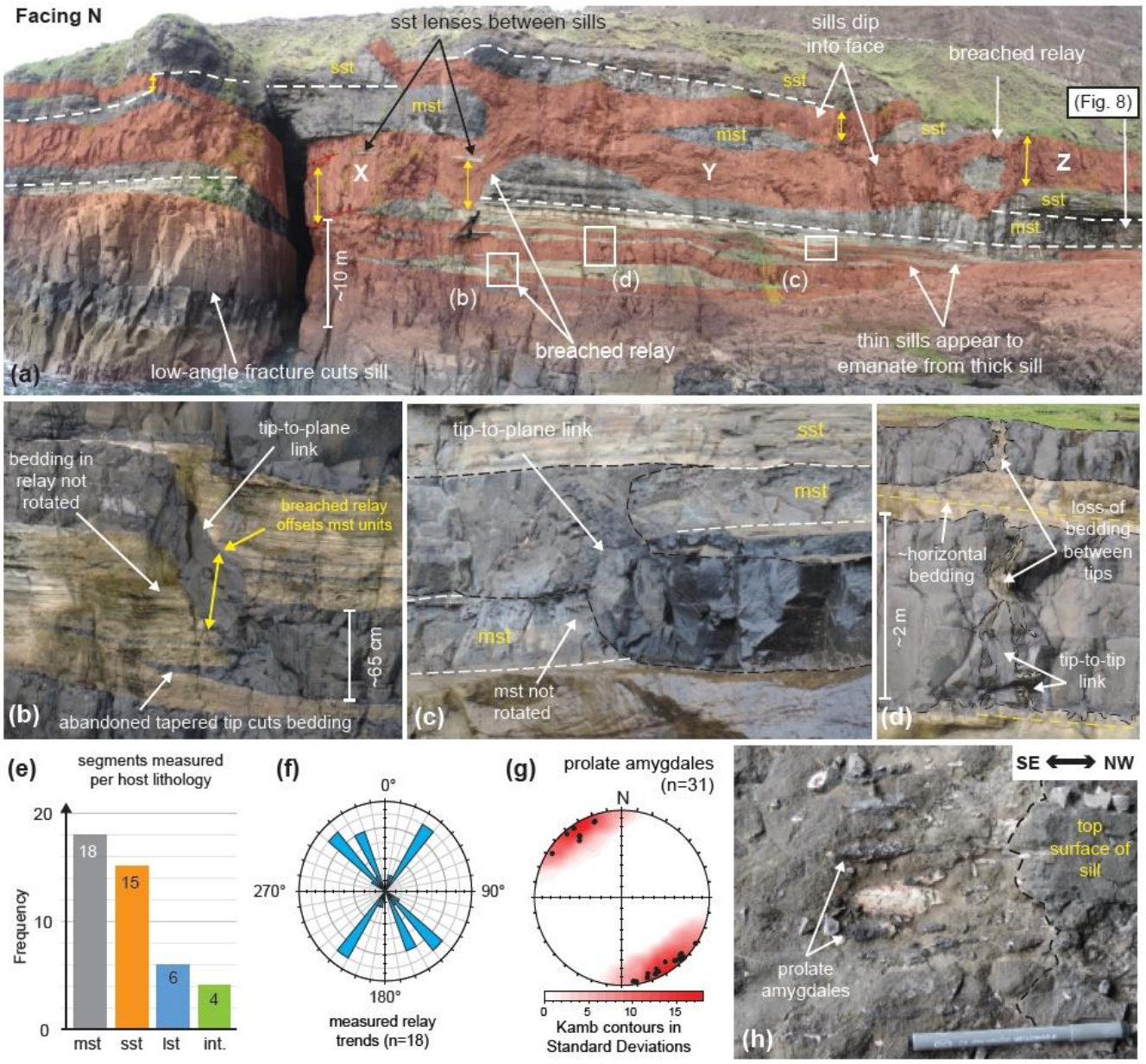

Figure 3. (a) Thin sill network in the Neist Point study area, sills display consistent near-vertical uplift of host rock (yellow arrows). Right-(NE)-stepping linked segments (X-Y-Z) transgress through mudstone and sandstone units at the tens-of-metre scale. Both En-echelon and collinear segment arrangements occur in the sandstone host rock: **(b)** tip-to-plane link, left-(SW)-stepping; **(c)** tip-to-plane link, left-(SW)-stepping; host rock is not rotated within these relays. **(d)** Collinear segments, host rock between tips has lost its primary structure (i.e. bedding). **(e)** Graph to show measured segments per host rock lithology. **(f)** Rose diagram showing relay trends in the study area, predominant trends are NW-SE and NE-SW; bins are split into 10° intervals and each bin represents 1 measurement. **(g)** Colour contoured equal area lower hemisphere stereonet of prolate amygdales at upper sill contact, plotted as lineations (measured as rake). **(h)** Example of prolate amygdales plotted in (g). (Unannotated photos available in Supplemental File 1, data available in Supplemental File 2).

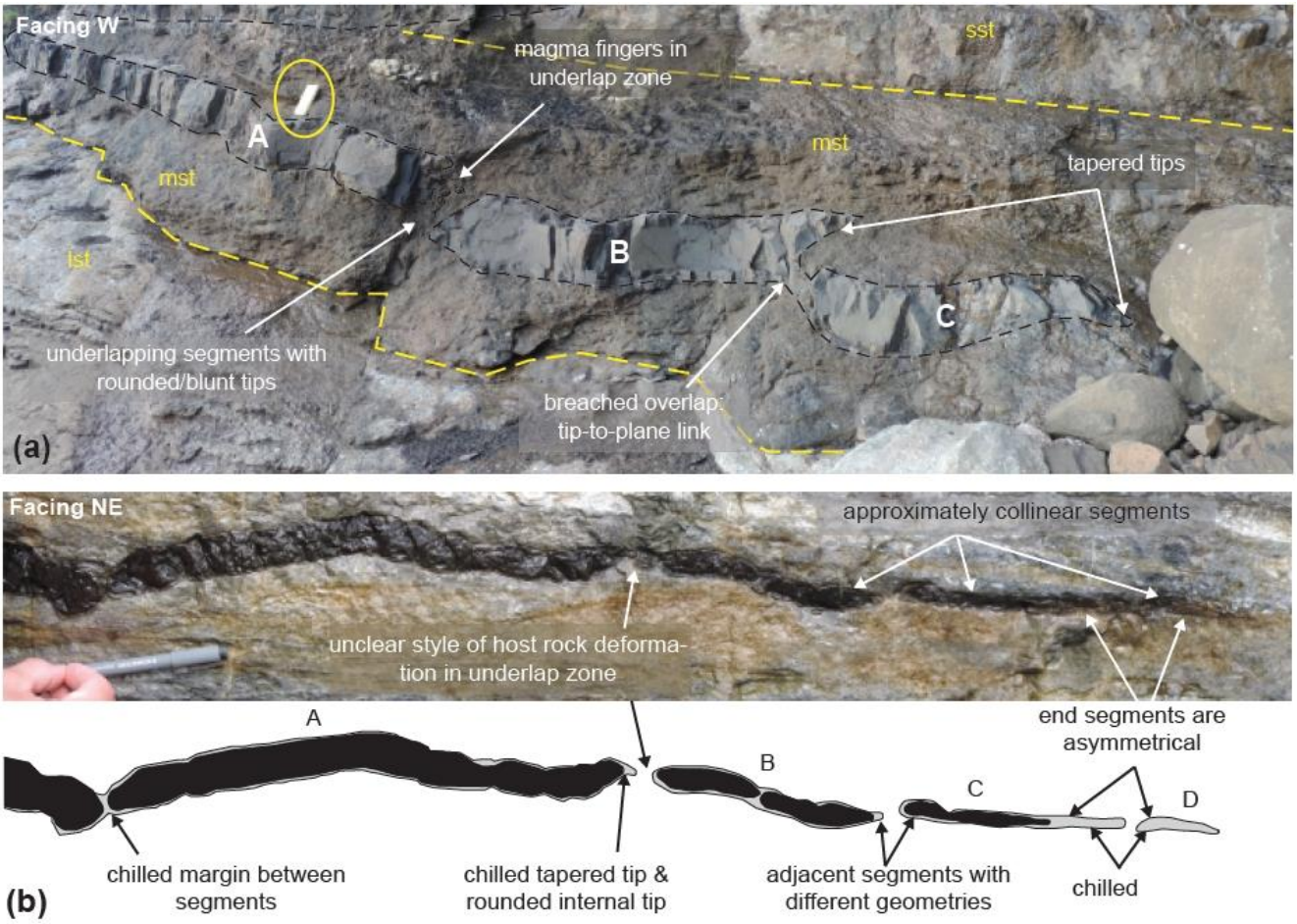

Figure 4. Examples of segment arrays in mudstone (a), and limestone (b). **(a)** Offset underlapping (segments A-B) and offset overlapping (segments B-C) arrangements in mudstone. **(b)** Photo and sketch of a colinear underlapping segment array in limestone. (Unannotated photos available in Supplemental File 1).

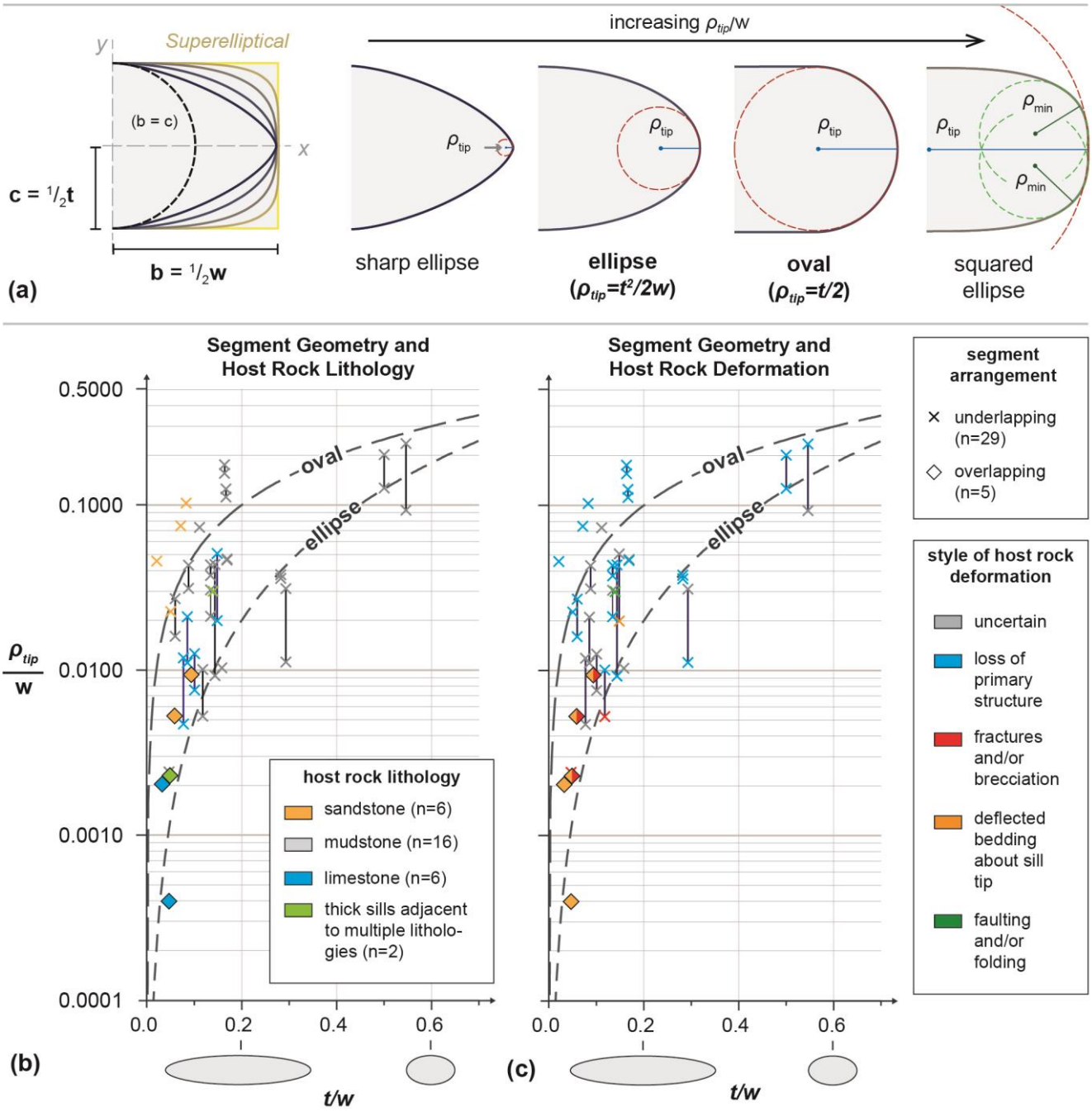

Figure 5. Geometrical characterisation of sill segment geometries in the Neist Point study area. (a) Schematic diagram to illustrate circular through to rectangular tip geometries and how the macro-tip form radius of curvature (ρ_{tip}; red circle) was measured. Note that once tip geometry surpasses an oval, corners develop and the superelliptical geometry can also be defined by two minimum radii of curvature (see green circles in "squared ellipse" example). Following the method of Pollard et al. [1975] the macro-tip forms were plotted to show: (b) segment geometry and host rock lithology; (c) segment geometry and observed style of localised host rock deformation ahead of the tip. Dashed lines for oval and elliptical geometries are shown for comparison to measured geometries. Individual segments are shown as two data points (denoting the geometry of each tip) connected by a line; line length correlates to the segment asymmetry about its c-axis (longer line = more asymmetric); isolated points are where only one tip could be measured. Symbols indicate segment arrangement (underlapping or overlapping). Note that schematic segments below the x-axis in (a) and (b) are to illustrate segment t/w ratio only. (Data available in Supplemental File 2).

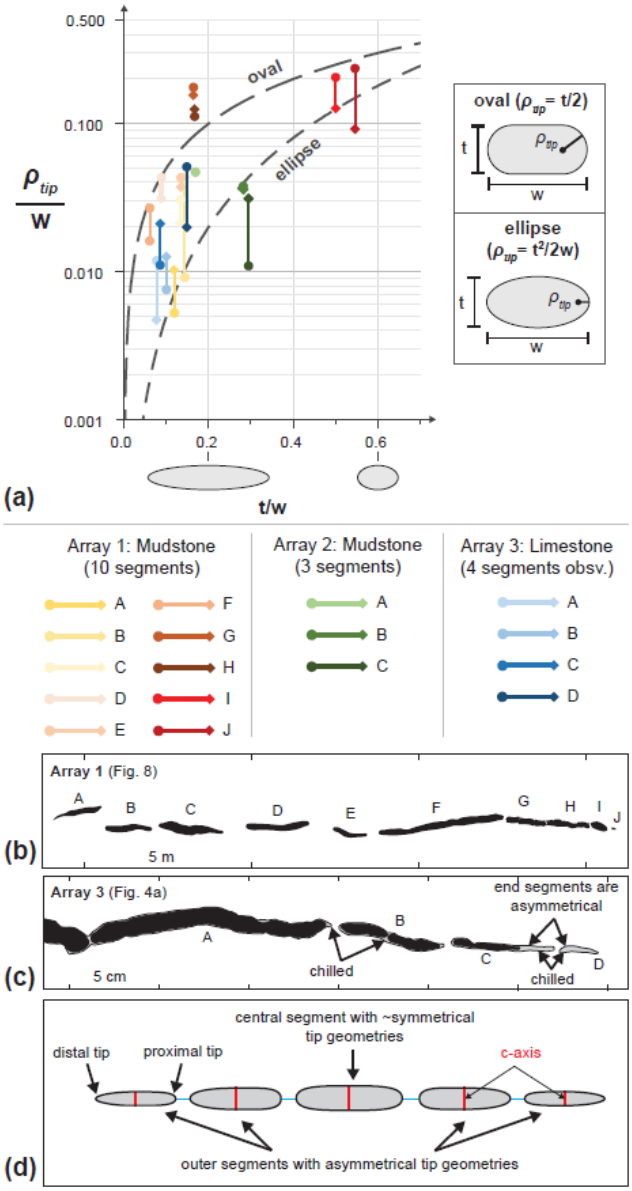

Figure 6. Geometrical characterization of individual segment geometries within an array. **(a)** Plot to define segment geometries: segment tips are displayed as circles and diamonds (for left and right tips, as observed in outcrop), individual segments are shown as linked symbols and the line length correlates to segment asymmetry about its c-axis (longer line = more asymmetric). Relay zones occur between the diamond and circle tips of adjacent segments (Data available in Supplemental File 2). Note that schematic segments below x-axis are to illustrate segment t/w ratio only. **(b-c)** Schematic sketches of two of the arrays: Array 1 (Fig. 8); Array 3 (Fig. 4b), only 4 segments were observed. **(d)** Illustration to show the generalised asymmetric geometry of collinear segments in an elastic medium (redrawn and modified from analogue model of Pollard et al. [1982]).

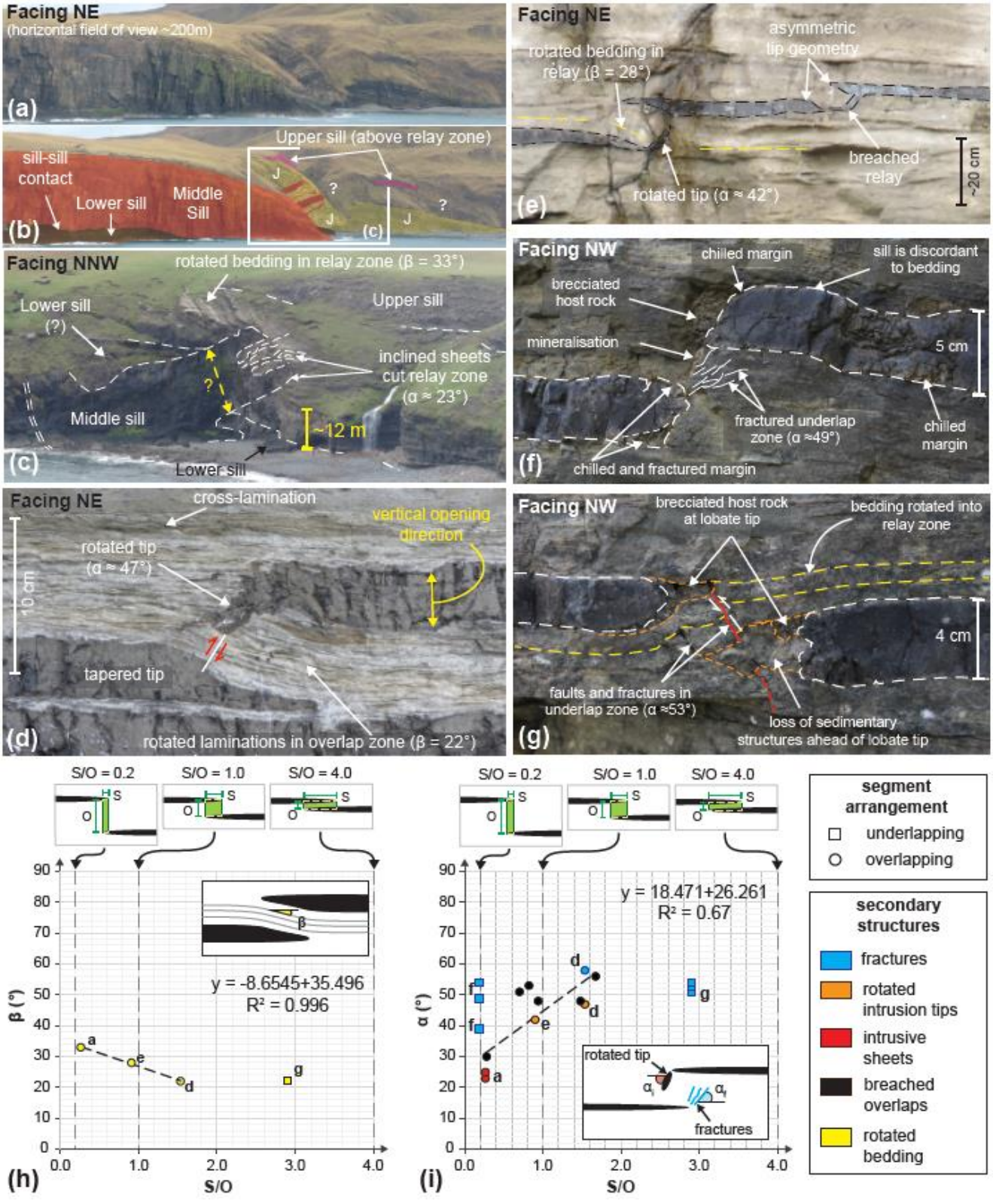

Figure 7. Overlap zones have comparable geometries across several orders of magnitude in the study area. **(a-c)** Tens-of-metre scale relay in interbedded sedimentary host, yellow arrow in (c) suggests the opening direction; Jurassic bedding is rotated in the overlap zone between two thick sills; sheets emanate from the lower sill tip and cut the relay zone. **(d)** Centimetre-scale relay in limestone; laminations are rotated between overlapping tips, fractures also cut the relay zone; the upper tips is rotated towards the lower segment. **(e)** Centimetre-scale relays in sandstone; overlap zone between left and central segments displays rotated bedding and the lower segment has a rotated tip; the central and right segments form a tip-

to-plane breached relay. **(f-g)** Underlapping segments in laminated sandstone at the East coast location (see Fig.6.1). **(f)** Rounded segments with chilled margins; brecciated and fractured host rock ahead each tip and within the relay zone. **(g)** Brecciation and loss of host rock structure ahead of rounded segment tips. (Unannotated photos (a-g) available in Supplemental File 1). **(h)** Graph to show rotation angle of bedding (β) in relay zones, plotted against relay aspect ratio (Separation/Offset); dashed line shows best-fit negative linear regression for overlap zones; underlap data is insufficient to determine a reliable relationship. **(i)** Graph to show the angle of secondary structures (α) within relay zones (i.e. fractures, rotated tips, or intrusive sheets), measured from the segment plane to the structure, plotted against relay zone aspect ratio (Separation/Offset); dashed line shows a best-fit positive linear regression for overlapping segments; underlap data is insufficient to determine a reliable relationship. Note, in (h) and (i), underlapping segments are plotted with positive S/O values. (Data for (h-I) available in Supplemental File 2).

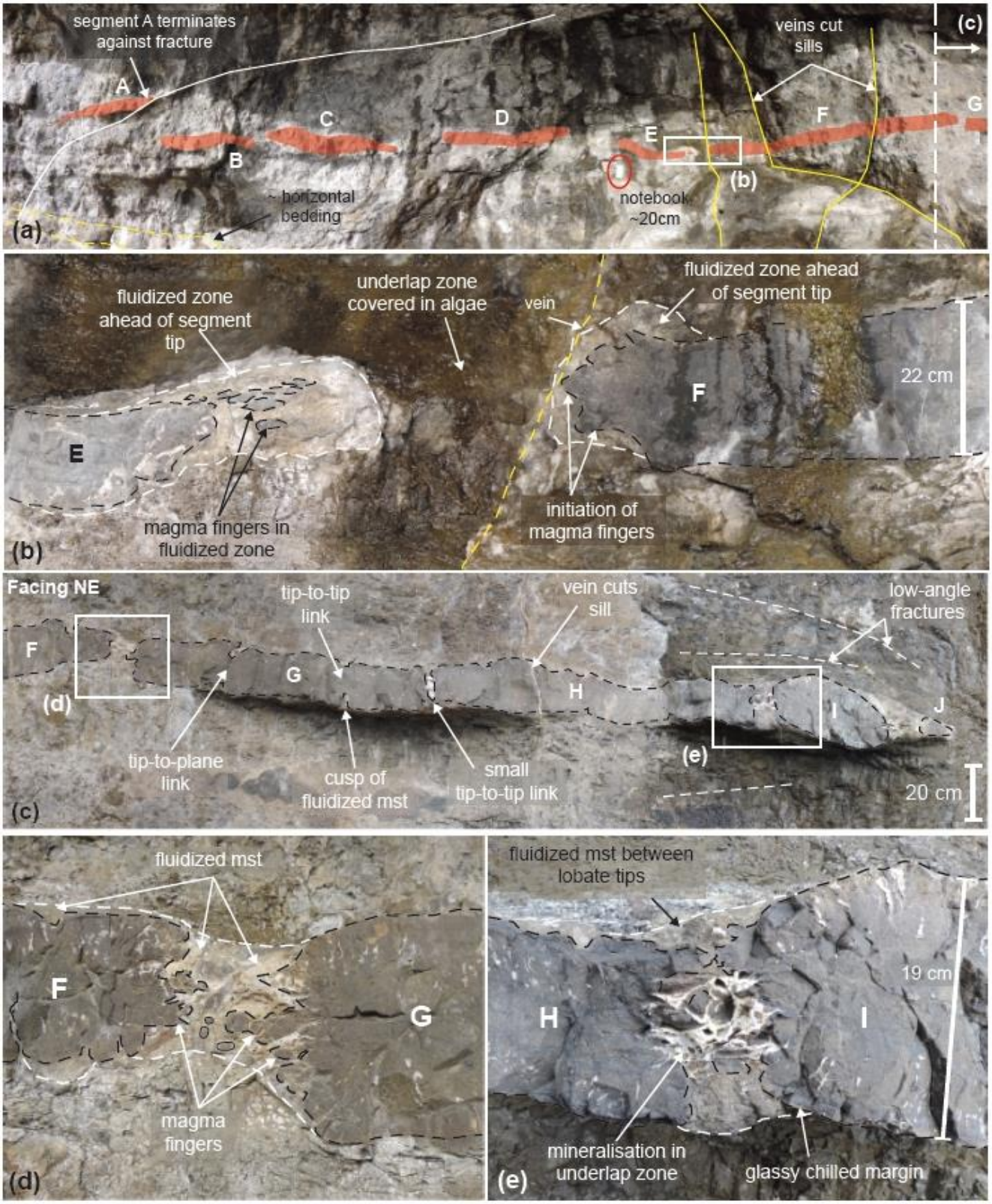

Figure 8. Photographs of an underlapping segment array in mudstone. **(a)** tens-of-metre segment array comprising offset and approximately collinear segments with inconsistent stepping directions; segments are coloured red and labelled A – F; array continues in (c). **(b)** Discoloured, fluidized zones ahead of segment E and F, fluidization does not appear to be continuous across the underlap zone. **(c)** Continuation of segment array in (a), showing segments F - J. **(d)** Discoloured, fluidized underlap zone between segments F and G. Magma fingers protrude from segment G towards F. **(e)** Discoloured, fluidized and mineralised underlap zone between segments H and I. (Unannotated photos available in Supplemental File 1).

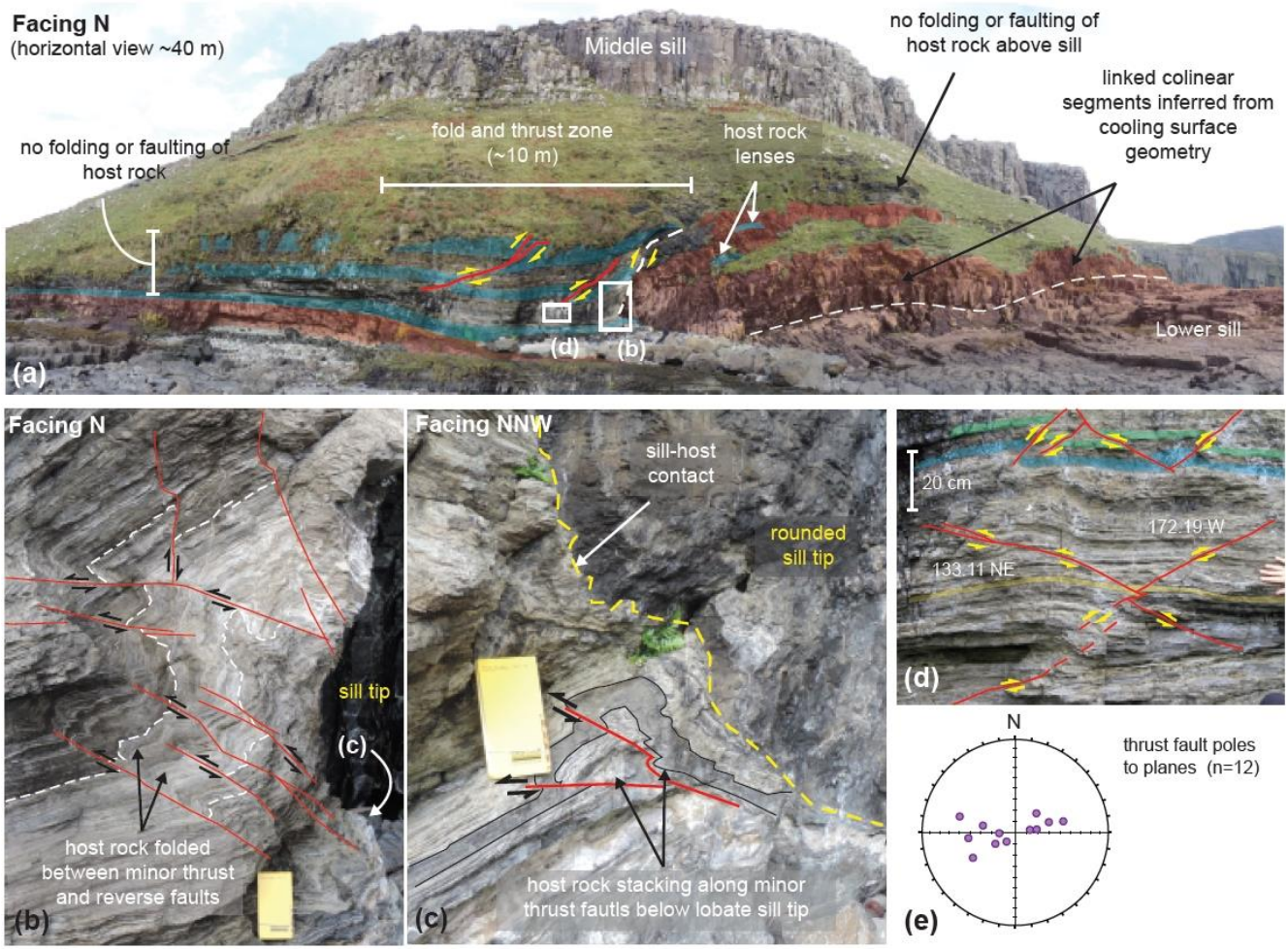

Figure 9. Fold and thrust zone ahead of a thick sill with a lobate sill tip (Location shown on Fig. 1). **(a)** Fold and thrust zone ahead of sill segment (highlighted red); marker units are highlighted blue. Major thrust faults verge towards the sill segment; exposed host units above the segment are not folded or faulted. **(b)** Minor thrust and reverse faults at the sill-host contact; notebook for scale. **(c)** Host rock stacking across thrust faults below the lobate tip; notebook for scale Centimetre-scale conjugate thrust faults below one of the major thrust faults. **(d)** Minor thrust and reverse faults at the sill-host contact; notebook for scale. (Unannotated photos (a-d) available in Supplemental File 1). **(e)** Equal-area lower-hemisphere projection with thrust faults ahead of the lobate tip plotted as poles to planes (Data available in Supplemental File 2).

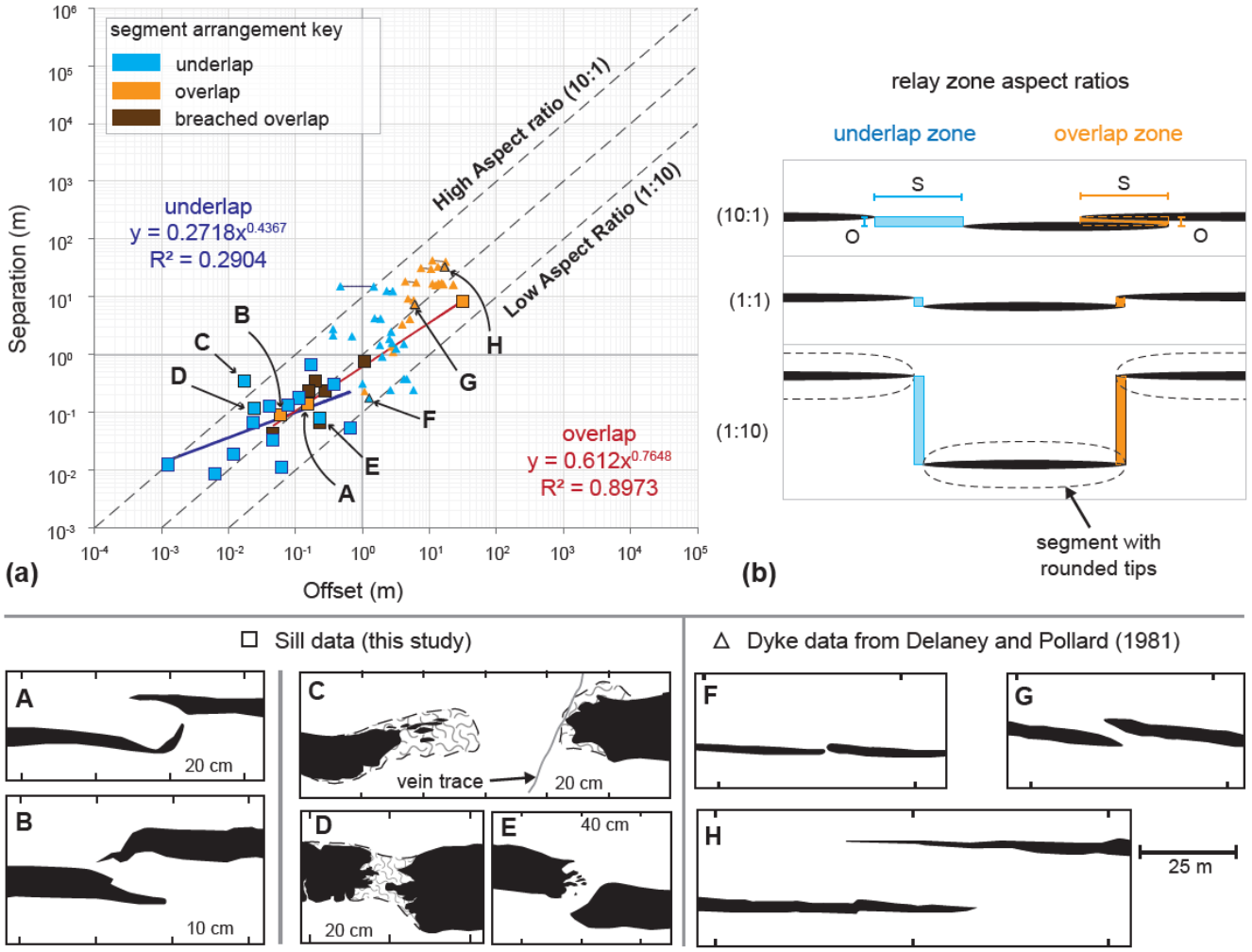

Figure 10. Geometrical characterization of relay zone aspect ratios between measured sill segments (Data available in Supplemental File 2). **(a)** Log-Log plot to show relay zone aspect ratios; collinear segments are not shown as zero-values cannot plot on a log-scale. **(b)** Illustrations of high (10:1), unity (1:1), and low (1:10) aspect ratios for underlapping and overlapping segments; separation, S; offset, O. Data in **(a)** shows relay zone geometry of underlapping (blue squares) and overlapping (orange squares) sill segments in the Neist Point study area. Low and high aspect ratio lines are from Long and Imber [2011]. Note that underlapping segments are plotted with positive values. Best fit power law regressions are fitted to the underlapping (blue line) and overlapping (red line) segments. The sill relay zone data is also plotted with published relay zone data for dykes intruded into shale at Ship Rock, New Mexico (triangles). The data was manually digitized from Delaney and Pollard [1981; their Fig.10] using WebPlotDigitizer, and replotted. Segment sketches A-E were drawn from examples in the Neist Point study area: A-B, overlapping and interacting; C-E, underlapping segments with rounded to blunt tips and minor magma fingers. Sketches of segment tip geometries (F-H) are also redrawn from Delaney and Pollard [1981; their Fig.10]: F, underlapping segments with rounded tips; G, slightly overlapping segments with asymmetrical tips, indicative of interaction; H, overlapping segments with symmetrical tapered tips, indicative of no segment interaction.

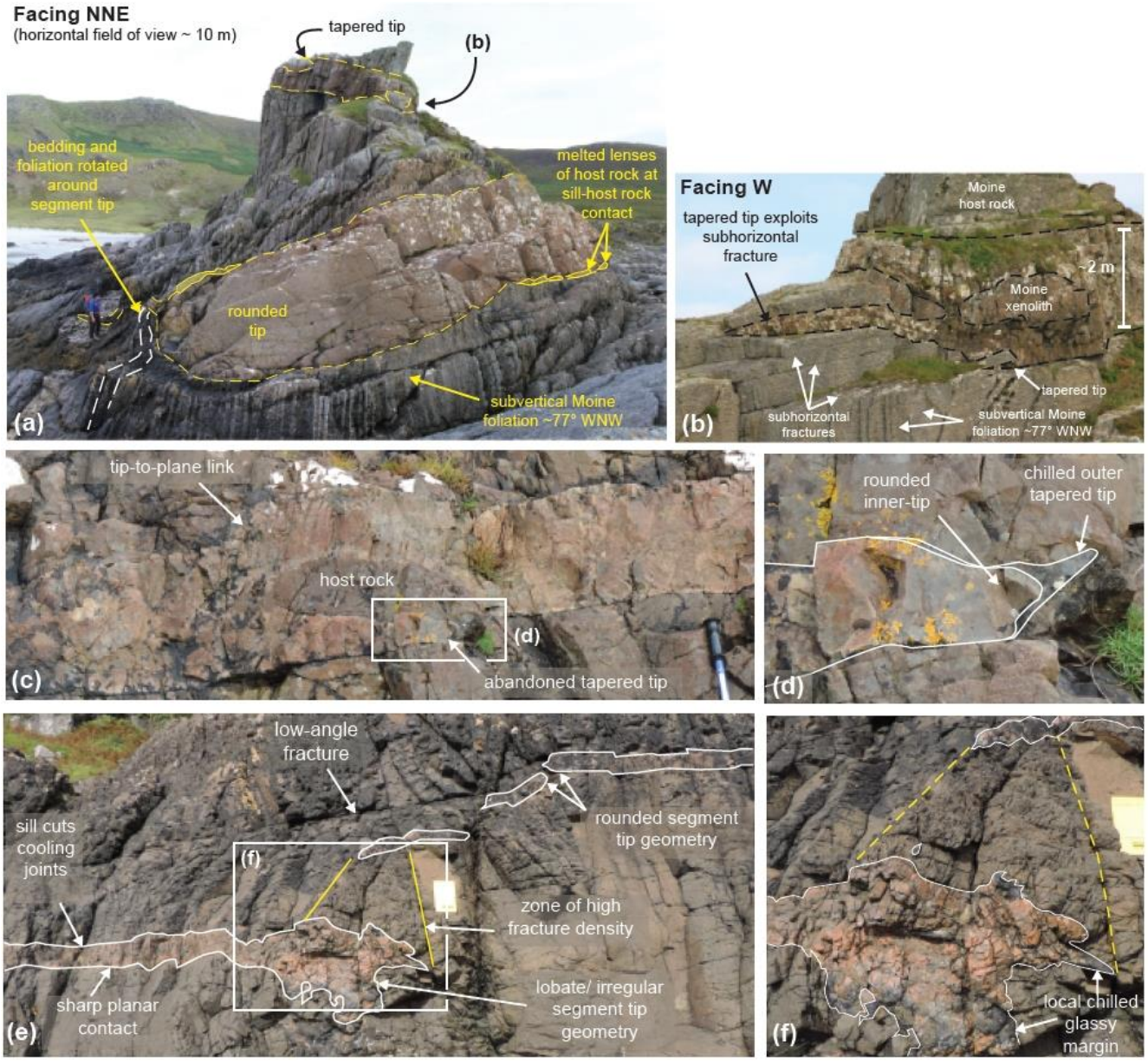

Figure 11. Segment tip geometries in the Loch Scridain Sill Complex, Isle of Mull, UK. **(a-b)** Segment geometry in sub-vertically bedded and foliated metasedimentary Moine basement; **(a)** Lower segment has a rounded tip, upper segment has a tapered tip, which is also shown in **(b)**. Tapered tips of upper segment exploit sub-horizontal fractures. **(c-f)** Sill segment geometry examples in the Paleocene Lava cover: **(c)** offset overlapping segments showing a tip-to-plane link, and an abandoned tapered tip. **(d)** zoom-in of abandoned tip showing outer chilled glassy margin and inner rounded tip geometry. **(e)** offset segments with sharp planar contacts; lower segment has a bulbous tip geometry with local irregularities associated with a highly fractured relay zone. **(f)** Zoom-in of the bulbous sill tip geometry. (Unannotated photos available in Supplemental File 1).

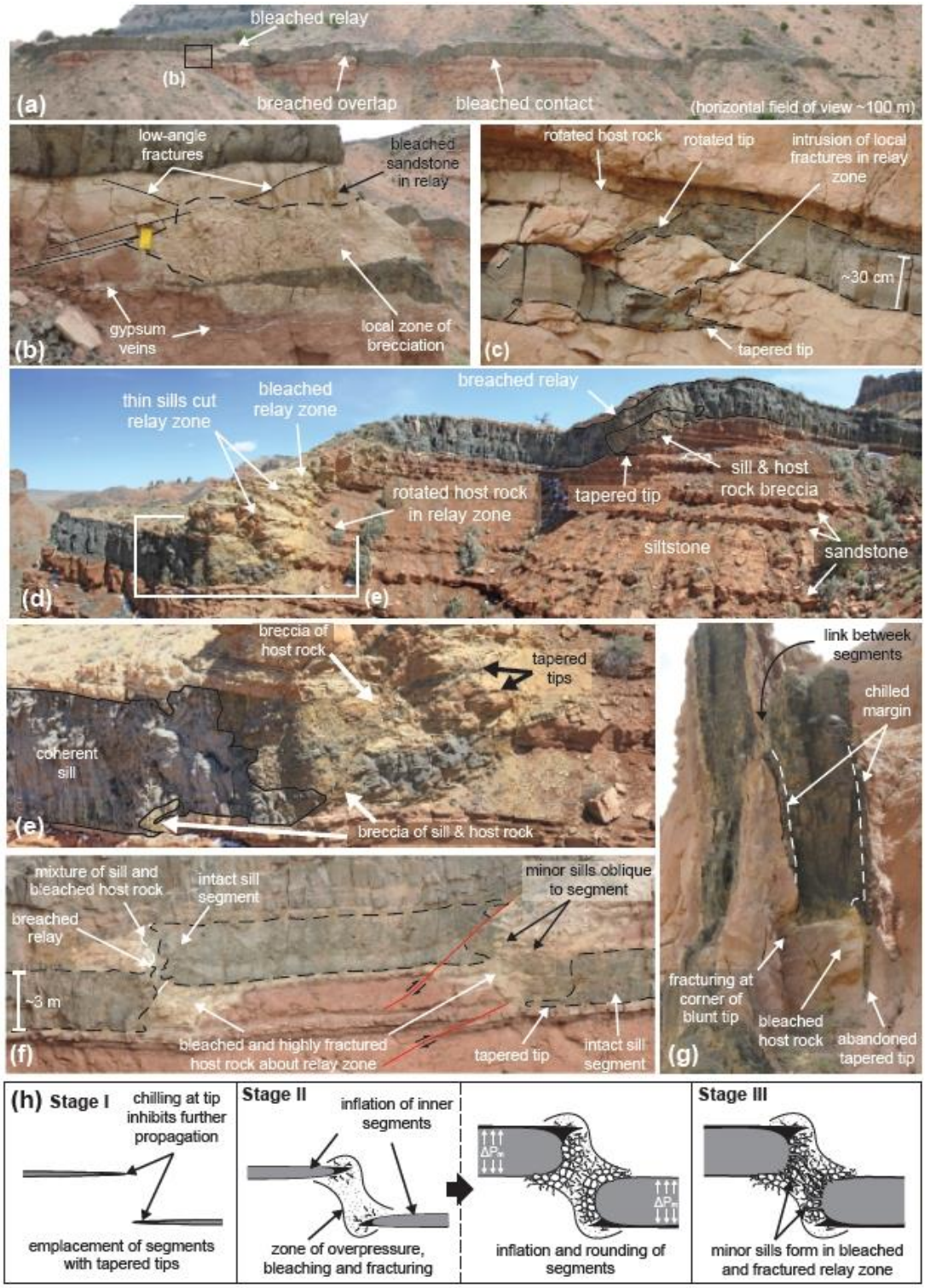

Figure 12. Field examples of offset overlapping and underlapping segments and breached relays in the SRSVF, Utah. (a) Overview photograph showing multiple linked segments and different styles of relay deformation: (b) bleached and highly fractured/brecciated relay zone, yellow notebook for scale; (c) rotated relay zone with oblique fractures, some have been intruded. (d) Un-breached and breached underlap zones between offset segments. (e) Thin sheets cut through bleached and brecciated underlap zone ahead of blunt sill tip. (f) Bleached, brecciated and heavily intruded relay zones between offset underlapping segments; the lower right segment has a chilled and abandoned tapered tip. (g) Example of segmented dykes in Utah showing chilled abandoned tapered tip and blunt (superellipse) segment geometry also associated with host rock bleaching and fracturing adjacent to blunt tip. (h) Schematic diagrams to illustrate how the sill and dyke segment geometries in the Utah study area likely developed. (Unannotated photos available in Supplemental File 1).

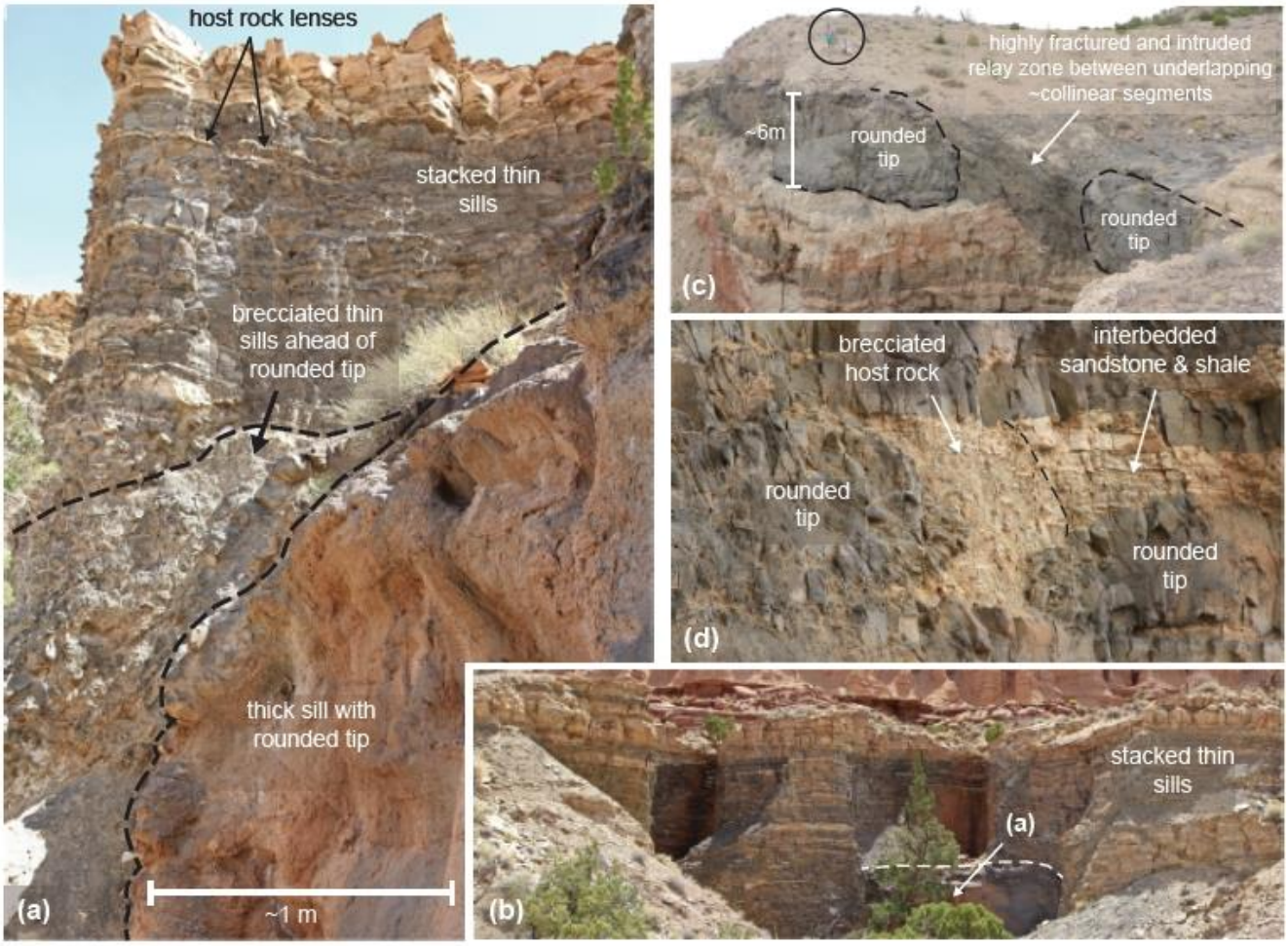

Figure 13. Collinear underlapping segments in the SRSVF, Utah. **(a)** Thick sill segment hosted in a stack of thin sills; thin sills ahead of rounded tip are brecciated. Location shown in **(b). (c)** Collinear underlapping segments with blunt tips and a heavily intruded underlap zone. **(d)** Collinear underlapping segments with rounded segment tips associated with a bleached and brecciated relay zone. (Unannotated photos available in Supplemental File 1).

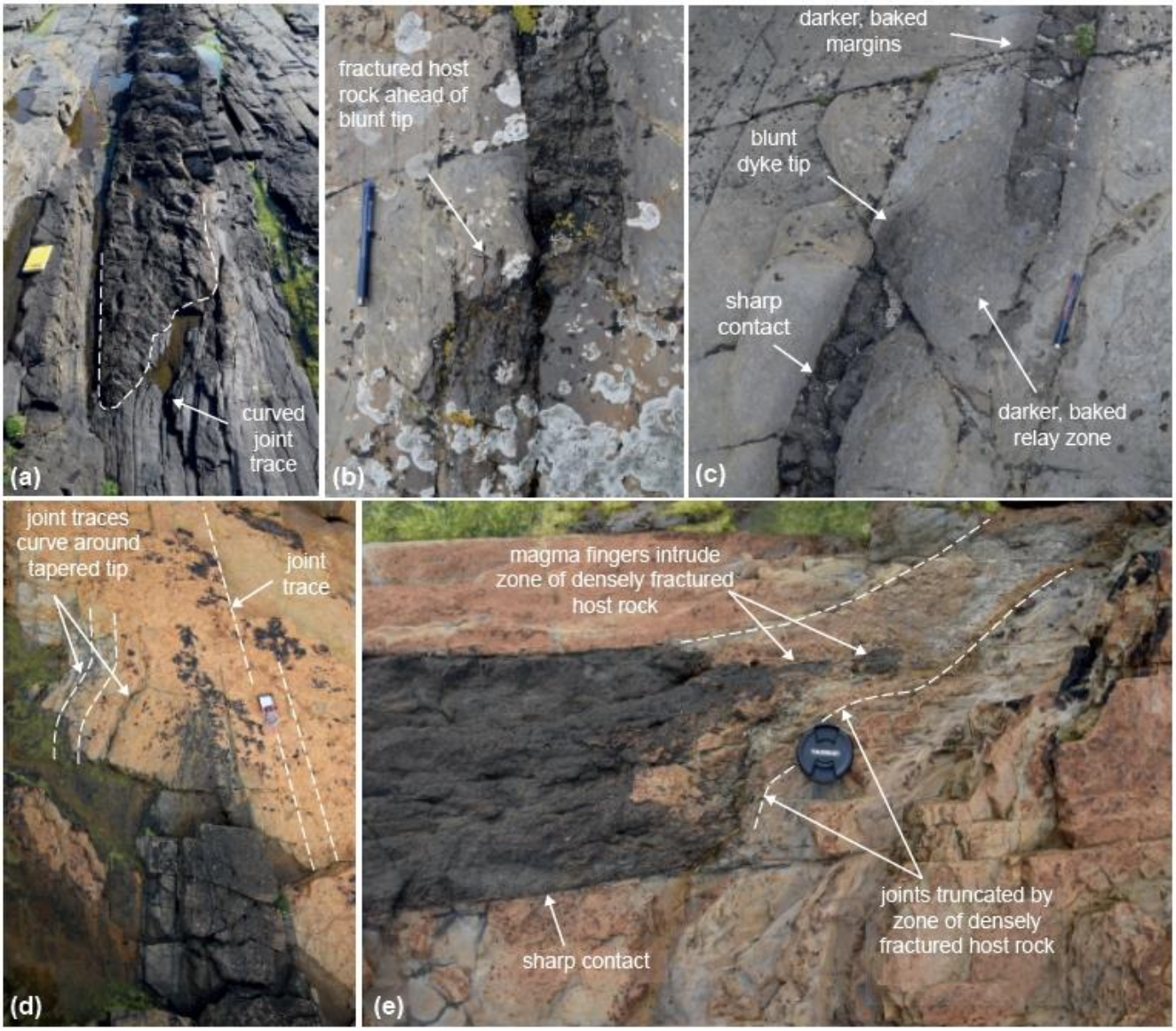

Figure 14. Field examples of segmented dykes and associated host rock deformation in mudstone (a-c) and siltstone (d-e) host rock at Birsay, Orkney, UK. **(a)** Joint traces curve around, and are truncated by, an asymmetrical tapered tip, notebook for scale. **(b)** Locally fractured host rock ahead of blunt (superellipse) underlapping dyke segments, pen for scale. **(c)** Baked host rock in relay zone between underlapping dyke segments with rounded tips; pen for scale. **(d)** Joint traces curve around asymmetrical tapered tip; compass for scale. **(e)** Joint traces truncated by highly fractured host rock ahead of blunt dyke tip. Magma fingers intrude the highly fractured zone, lens cap for scale. (Unannotated photos available in Supplemental File 1).

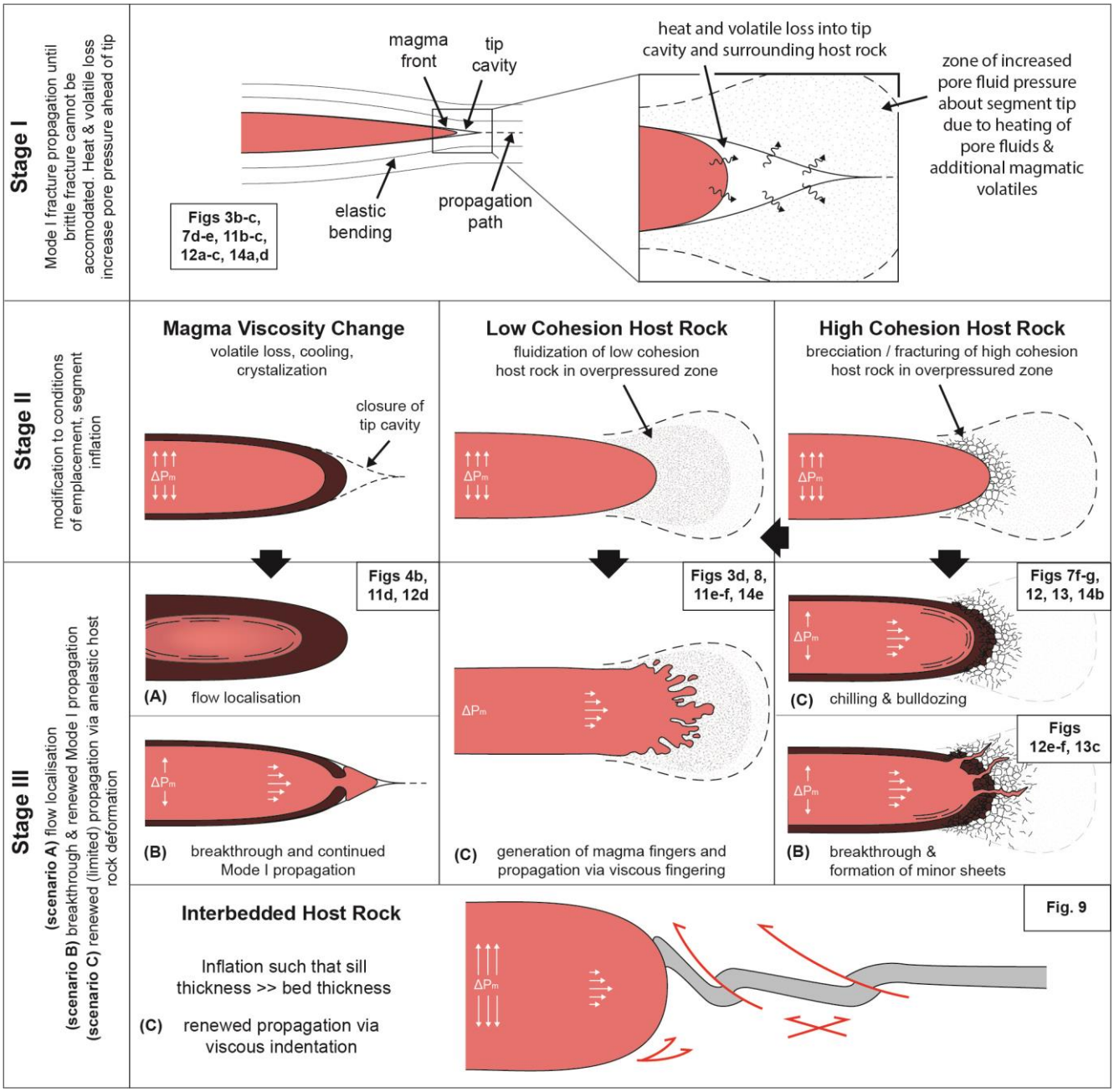

Figure 15. Conceptual model for evolution of collinear segments. **(a)** Stage I: Brittle propagation; **(b)** Stage II: local modification to the conditions of emplacement; driving pressure is accommodated predominantly by segment inflation. With increased fluid pressure, disaggregated (brecciated / fractured) high cohesion host rock could become fluidized, or disaggregated host may behave as a viscous medium. **(c)** Stage III: renewed limited propagation via anelastic propagation mechanisms.